Wake topology and hydrodynamic performance of low-aspect-ratio flapping foils

By H. DONG[1], R. MITTAL[1] AND F. M. NAJJAR[2]

[1]Department of Mechanical and Aerospace Engineering, The George Washington University,
801 22nd St. NW, Washington, DC 20052, USA

[2]Centre For Simulation of Advanced Rockets, University of Illinois at Urbana-Champaign,
Urbana, IL 61801, USA

Numerical simulations are used to investigate the effect of aspect ratio on the wake topology and hydrodynamic performance of thin ellipsoidal flapping foils. The study is motivated by the quest to understand the hydrodynamics of fish pectoral fins. The simulations employ an immersed boundary method that allows us to simulate flows with complex moving boundaries on fixed Cartesian grids. A detailed analysis of the vortex topology shows that the wake of low-aspect-ratio flapping foils is dominated by two sets of interconnected vortex loops that evolve into distinct vortex rings as they convect downstream. The flow downstream of these flapping foils is characterized by two oblique jets and the implications of this characteristic on the hydrodynamic performance are examined. Simulations are also used to examine the thrust and propulsive efficiency of these foils over a range of Strouhal and Reynolds numbers as well as pitch-bias angles.

1. Introduction

The term 'flapping' is usually applied in the context of the wing motion of birds and insects and consists of an oscillatory rolling motion of the wing about the shoulder joint with simultaneous change in the geometric pitch angle of the wing via a rotation of the wing about its spanwise axis. Pectoral fins of fish also exhibit essentially similar kinematics although large-scale passive as well as active deformation of these fins can significantly increase the complexity of the fin kinematics. In many studies, this so-called 'pitching and rolling' motion has been simplified to a 'pitching and heaving' motion wherein the rolling motion of the wing is replaced by a heaving motion. In addition to serving as a model for flapping wing/fin kinematics, pitch-and-heave also represents the essential kinematics of caudal-fin motion in carangiform propulsion (Lighthill 1975).

Past studies have successfully employed pitching-and-heaving foils as models of flapping wings and gained useful insight into the fluid dynamics of flapping flight as well as carangiform propulsion. Most of these past studies have assumed that the aspect ratio of the foils is large and have therefore restricted their attention to two-dimensional flapping foil configurations. In experimental studies, this has been accomplished through the use of high-aspect-ratio foils (Koochesfahani 1989; Triantafyllou, Triantafyllou & Grosenbaugh 1992) whereas numerical studies accomplish this by explicitly performing two-dimensional simulations that ignore any spanwise variability in the foil geometry and the flow field (Jones, Dohring & Platzer 1998; Isogai, Shinmoto & Watanabe 1999; Tuncer & Platzer 2000; Wang 2000;

Mittal, Uttukar & Udaykumar 2002*a*; Mittal *et al.* 2003; Lewin & Haj-Hariri 2003; Pedro, Suleman & Djilali 2003; Guglielmini & Blondeaux 2004).

The assumption of two-dimensionality has some validity for bird and insect flight where wings of many species tend to be of a relatively large aspect ratio. For instance, even a small bird such as a tree sparrow has a wing with an aspect ratio (denoted by symbol $Æ\!R$ and defined as $(\text{span})^2/(\text{area})$) of about 5 (Azuma 1992). Aspect ratio for soaring birds such as albatrosses can reach values as high as 18. Examples of relatively high-aspect-ratio wings also abound in the insect world; for instance, the aspect ratio of a bumblebee wing is about 6.3 (Usherwood & Ellington 2002) and that of craneflies is about 11 (Ellington 1984). In contrast, the aspect ratio of fish pectoral fins tend to be generally smaller. For instance, the aspect ratios of four species of labrid fishes range from about 1.5 to 3.5 (Walker & Westneat 2002), whereas bluegill sunfish and ratfish have pectoral fins with aspect ratios of about 2.4 (Drucker & Lauder 1999) and 2.2 (Combes & Daniel 2001), respectively. Evolutionary pressure towards these smaller-aspect-ratios in pectoral fins is probably due to a number of different factors. Smaller fish that live in highly energetic habitats such as coral reefs and near-shore regions make extensive use of pectoral fins for propulsion as well as manoeuvring and station-keeping. As discussed extensively by Walker & Westneat (2002), the pectoral fin kinematics adopted by these fish can range all the way from a back-and-forth paddle-like motion (for braking, turning and fast starts) to flapping motion (for cruising). It has generally been understood that propulsive forces in paddling are drag-based for which low aspect-ratio fins are most appropriate. In contrast, flapping motion is considered to be associated with lift-based propulsion and this is expected to work best with higher-aspect-ratio wings/fins (Combes & Daniel 2001; Walker & Westneat 2002). Thus, just from a hydrodynamic point of view, fish pectoral fins would tend to be of a lower aspect ratio than insect and bird wings. In addition, large-aspect-ratio fins would require a stiffer and therefore heavier fin support structure since they would be subject to larger bending moments.

In this context, it might also be argued that the abundance of high-aspect-ratio wings in flying animals and the contrasting paucity of high-aspect-ratio pectoral fins in fish is primarily connected with water being three-orders of magnitude denser than air. A flapping fish fin would therefore experience significantly higher added-mass associated bending moments and a lower aspect ratio would tend to reduce this bending moment for fish fins. However, many insects such as wasps, flies and bubblebees routinely flap their wings at frequencies exceeding 150 Hz (Azuma 1992) whereas flapping frequencies of fish pectoral fins seldom exceed 5 Hz (Drucker & Lauder 1999; Walker & Westneat 2002). Since the added-mass force is proportional to the square of the flapping frequency, it is easy to see that added-mass associated moments experienced by the wings of many flying insects could be comparable with those experienced by the pectoral fins of fish. Thus in our view, added-mass force although important, is not the primary determining factor of fish-fin aspect ratio.

In addition to the above hydrodynamic factors, there are probably many non-hydrodynamic factors that produce pressure towards smaller-aspect-ratio pectoral fins. For instance, high-aspect-ratio fins have a larger visual signature and would also be cumbersome to operate in tight spaces. The key question then becomes: how well do these relatively low-aspect-ratio fins work when used during flapping and how does their performance vary with aspect ratio and other key kinematic parameters? These same questions are also relevant for underwater vehicles that are designed to use flapping foil propulsors (Fish *et al.* 2003; Techet *et al.* 2005). Large-aspect-ratio foils are cumbersome to operate in complex environments, are more prone

to damage and also require a stronger and heavier support structure to withstand the larger bending moments. Thus, it is of interest to assess the hydrodynamic performance deterioration that is associated with the use of low-aspect-ratio foils. Finally, many studies have shown that the wake structure is a critical determinant of the hydrodynamic performance of flapping foils. However, relatively little is known about the wake topology of finite and low-ratio foils. A systematic and comprehensive examination of the hydrodynamics of small-aspect-ratio ($\mathcal{R} \leqslant 5$) flapping foils would allow us to gain some insight into all these issues and this forms one motivation for the current study.

A number of studies have examined the fluid dynamics and force production of finite aspect-ratio flapping foils/wings. Usherwood & Ellington (2002) have studied the fluid dynamics of a hawkmoth wing model of aspect ratio 6.34 and numerical simulations of this same wing have been carried out by Liu *et al.* (1998). Dickinson and co-workers (Dickinson, Lehmann & Sane 1999; Sane & Dickinson 2001) have performed systematic experimental studies with a dynamically scaled fruitfly flapping wing with aspect ratio of about 3.8 and Ramamurti & Sandberg (2002) and Sun & Tang (2002) have used this same wing in their numerical simulations. Techet *et al.* (2005) have examined the thrust performance of a three-dimensional flapping foil with an aspect ratio of 4.5.

Detailed experiments of pectoral fin hydrodynamics in controlled experiments with swimming fish have also been carried out (Walker & Westneat 1997; Drucker & Lauder 2002). The comprehensive particle image velocimetry (PIV) measurements carried out for a swimming bluegill sunfish (Drucker & Lauder 2002; Lauder *et al.* 2005) are of particular interest for the current study. In these experiments, the fish swims almost steadily in an incoming stream using only its pectoral fins. That the fish is swimming at very nearly a constant speed is confirmed by the fact that the body of the fish maintains its position to within a few millimetres over many fin strokes (Lauder *et al.* 2005). Thus, in this situation, the thrust produced by the fin is almost exactly balanced by the drag on the body of the fish. In this mode, fin hydrodynamics is primarily determined by the fin flapping frequency, fin amplitude and the flow speed which can be expressed in terms of a fin Strouhal number, normalized amplitude and fin Reynolds number. In general, for fish with different sizes and swimming speeds, these three non-dimensional parameters can vary over a wide range. Because of this, most studies that attempt to gain general insights into the performance of fins, flapping foils or flapping wings find it convenient to examine the problem in terms of these non-dimensional parameters (Freymuth 1988; Triantafyllou *et al.* 1992; Anderson *et al.* 1998; Walker & Westneat 2000; Wang 2000; Combes & Daniel 2001; von Ellenrieder, Parker & Soria 2003; Lewin & Haj-Hariri 2003; Prempraneerach, Hover & Triantafyllou 2003; Hover, Haugsdal & Triantafyllou 2004; Blondeaux *et al.* 2005*a*, *b*; Techet *et al.* 2005) since this allows for the study of the flapping appendage without regard to the associated body. We have adopted a similar approach in the current study.

In the particular case of labriform propulsion, since the very near wake of the pectoral fin is not affected by the wake of the fish body, the fin near-wake can be examined in order to assess the thrust production of the fin. The study of Drucker & Lauder (2002) showed that the pectoral fins of the sunfish produce a train of vortex rings which are associated with momentum addition in the fin wake and consequently to a production of force on the fin. Through modification in the fin gait, the fish can alter the axis and direction of travel of these vortex rings and through this, control the direction and magnitude of the forces and moments on the fin. Ramamurti *et al.* (2002) simulated the flow associated with the pectoral fin of a bird-wrasse which was

the subject of the study by Walker & Westneat (1997) and examined in detail the flow structure and force production of this fin.

Von Ellenrieder *et al.* (2003) examined the flow associated with a rectangular flapping foil of aspect ratio 3.0 at a Reynolds number of 163. The Strouhal number in this study varies from 0.2 to 0.35 and pitch angle amplitude from 0° to 20°. The dye visualization study of von Ellenrieder *et al.* (2003) was conducted over a range of flapping amplitudes and frequencies and the effect of these parameters on the vortex topology was elucidated. They found that the wake of these flapping foils was dominated by sets of loops and rings and they describe the evolution of these vortex structures. This configuration was studied numerically by Blondeaux and co-workers (Guglielmini & Blondeaux 2004; Blondeaux *et al.* 2005*a*, *b*). Blondeaux *et al.* (2005*a*, *b*) have examined the wake evolution at Strouhal numbers of 0.175 and 0.35 and the simulations show that a vortex ring is shed every half-cycle from the flapping foil. Also, Blondeaux *et al.* (2005*a*, *b*) indicate that as the Strouhal number is increased, there is an increased interaction between adjacent rings. The vortex structures in the numerical study were found to be different from those observed in the experiments of von Ellenrieder *et al.* (2003). In particular, Blondeaux *et al.* (2005*a*, *b*) point out that in contrast to the experiments, the simulations do not show the presence of distinct vortex loops in the wake associated with the trailing-edge vortex. Neither the experiments nor any of these simulations have examined the force generation by this flapping foil, therefore it is not clear if the foils are indeed generating thrust.

Buckholtz & Smits (2006) is also of relevance to the current study. In this study, flow visualizations are used to examine the wake of a low-aspect-ratio pitching panel. The Strouhal number of the panel was 0.23 and the chord-based Reynolds number was 640. The experiments showed that the wake of the panel was dominated by vortex loops of alternating sign and a vortex skeleton model was proposed for the wake formation. Buckholtz & Smits (2006) also observe that despite the lack of a leading edge, the wake behaviour is similar to that observed by Guglielmini & Blondeaux (2004) for a pitching–heaving foil. This indicates that the underlying vortex dynamics of these configurations is quite robust.

Despite all of these previous works on finite aspect-ratio flapping foils/wings, the number of studies that have systematically examined the effect of aspect ratio on the fluid dynamics and force production of low-aspect-ratio foils is limited. Ahmadi & Widnall (1986) used a linearized low-frequency unsteady lifting line theory to examine the energetics of wings undergoing a combined pitch-and-heave motion. Aspect ratios in their study varied from 8 to 16. Cheng, Zhuang & Tong (1991) used an unsteady vortex ring panel method to study the energetics and force production of undulating plates with aspect ratios ranging from 0.5 to 8.0. A key finding in their study was that the undulatory motion can reduce three-dimensional effects and lead to good swimming performance. Usherwood & Ellington (2002) have examined the effect of aspect ratio on the force generation by a rotating wing based on a hawkmoth wing. The emphasis of this study was on insect and bird flight and the aspect ratios in their study varied from 4.53 to 15.84. Mittal *et al.* (2003) used Navier–Stokes simulations to examine the wake vortex topology for foils with aspect ratios of 1.27 and 2.55 undergoing a sinusoidal heaving motion at a Reynolds number of 100. They found that the wake of these foils was dominated by two sets of interconnected vortex rings that convect at an oblique angle to the wake centreline.

A study that requires special mention here is that of Combes & Daniel (2001) who have examined the effect of aspect ratio and fin planform on the hydrodynamic performance of fins modelled after ratfish pectoral fins. They employ unsteady

potential theory to predict the thrust and efficiency of wings of aspect ratios ranging from about 0.1 to higher than 10. The simulations do not include any tip effects since the model employed does not account for spanwise flow variations, but nevertheless, their calculation show that while thrust increases monotonically with aspect ratio, efficiency has non-monotonic variation up to aspect ratios of about 2 and a monotonic increase beyond that. Based on this analysis, Combes & Daniel (2001) attempt to explain the wide variety of fin kinematics and morphologies that are observed in nature.

In the current numerical study, we perform a comprehensive analysis of the wake topology, force production and energetics of ellipsoidal flapping foils over a range of aspect ratios ($A\!R$), Strouhal frequencies (St), Reynolds numbers (Re) and pitch-bias angles. The primary motivation is to provide fundamental insights into the fluid dynamics of low-aspect-ratio thrust flapping foils and supplement the extensive work that has been done in the past on two-dimensional flapping foils. The full three-dimensional Navier–Stokes equations are solved numerically here and therefore, all unsteady–viscous and spanwise effects are included. Aspect ratios in the current study range from 1.27 to 5.09 which cover the range most relevant to pectoral fin propulsion. A two-dimensional ($A\!R = \infty$) case is also simulated for comparison. We begin by describing the simulation methodology and results of a systematic grid and domain dependence study. This is followed by a detailed discussion of the wake vortex topology as well as mean wake features observed over the range of the parameters varied in the current study. Finally, we present results on hydrodynamic performance of these flapping foil and based on this, speculate on how hydrodynamic performance might produce pressure towards pectoral fins in fish with certain aspect ratios.

In making connections between the current study and fish pectoral fins, it is important to take note of some of the features of fish pectoral fins that are not included in the current configuration. As pointed out previously, flapping is more accurately modelled as a pitching–rolling motion and the current pitching–heaving motion can be considered a simplification of this motion. Secondly, fish pectoral fins can range from relatively stiff (Walker & Westneat 1997; Combes & Daniel 2001) to highly flexible (Lauder *et al.* 2005) which can undergo passive as well as active deformation during flapping. Finally, even among labriform swimmers, pectoral fins have a very large variety of shapes and sizes. Since no one study could possibly examine pectoral fins in all their generality and complexity, the only way to distill some general insights is to work with a simple model of the configuration. In the current study, we focus on one shape metric of foils/fins, the aspect ratio, and examine thoroughly the effect of this parameter on the thrust performance. Thus all these limitations must be kept in mind while interpreting the results of the current study in the context of fish pectoral fins and later in the paper, we comment specifically on some of these limitations. It should also be re-emphasized that the current study also has relevance to engineered flapping foils. Engineered flapping foils are mostly rigid (Techet *et al.* 2005) and have relatively simple planforms and therefore the current study provides data and insights that are useful for such foils also.

2. Numerical simulation procedure

2.1. *Governing equations and numerical method*

The equations governing this flow are the three-dimensional unsteady, viscous incompressible Navier–Stokes equations

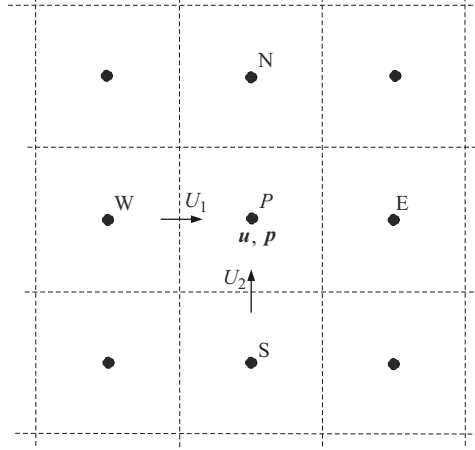$$\frac{\partial u_i}{\partial x_i} = 0, \qquad (2.1a)$$

FIGURE 1. Schematic describing spatial discretization.

$$\frac{\partial u_i}{\partial t} + \frac{\partial (u_i u_j)}{\partial x_j} = -\frac{1}{\rho}\frac{\partial p}{\partial x_i} + \nu \frac{\partial}{\partial x_j}\left(\frac{\partial u_i}{\partial x_j}\right), \tag{2.1b}$$

where u_i are the velocity components, p is the pressure, and ρ and ν are the fluid density and kinematic viscosity, respectively.

The Navier–Stokes equations (2.1) are discretized using a cell-centred, collocated (non-staggered) arrangement of the primitive variables (u_i, p). In addition to the cell-centre velocities (u_i), the face-centre velocities, U_i, are computed. The equations are integrated in time using the fractional step method of Van-Kan (1986). In the first sub-step of this method, a modified momentum equation is solved and an intermediate velocity u_i^* obtained. A second-order Adams–Bashforth scheme is employed for the convective terms while the diffusion terms are discretized using an implicit Crank–Nicolson scheme which eliminates the viscous stability constraint. In this sub-step, the following modified momentum equation is solved at the cell-nodes

$$\frac{u_i^* - u_i^n}{\Delta t} + \tfrac{1}{2}\left[3N_i^n - N_i^{n-1}\right] = -\frac{1}{\rho}\frac{\delta p^n}{\delta x_i} + \tfrac{1}{2}\left(D_i^* + D_i^n\right), \tag{2.2}$$

where $N_i = \delta(U_j u_i)/\delta x_j$, $D_i = \nu(\delta/\delta x_j)(\delta u_i/\delta x_j)$ and $\delta/\delta x$ corresponds to a second-order central difference. This equation is solved using a line-SOR scheme. Subsequently, face-centre velocities at this intermediate step, U_i^*, are computed by averaging the corresponding values at the grid nodes. Similar to a fully staggered arrangement, only the face velocity component normal to the cell-face is calculated and used for computing the volume flux from each cell. With reference to figure 1 for a two-dimensional case, the following averaging procedure is followed;

$$\widetilde{u}_i = u_i^* + \Delta t \frac{1}{\rho}\left(\frac{\delta p^n}{\delta x_i}\right)_{cc}, \tag{2.3a}$$

$$\widetilde{U}_1 = \gamma_w \widetilde{u}_{1P} + (1 - \gamma_w)\widetilde{u}_{1W}, \tag{2.3b}$$

$$\widetilde{U}_2 = \gamma_s \widetilde{u}_{2P} + (1 - \gamma_s)\widetilde{u}_{2S}, \tag{2.3c}$$

$$U_i^* = \widetilde{U}_i - \Delta t \frac{1}{\rho}\left(\frac{\delta p^n}{\delta x_i}\right)_{fc}, \tag{2.3d}$$

where γ_w and γ_s are the weights corresponding to linear interpolation for the west and south face velocity components, respectively. Furthermore, cc and fc denote gradients computed at cell-centres and face-centres, respectively. The above procedure is necessary to eliminate odd–even decoupling that usually occurs with non-staggered methods and which leads to large pressure variations in space. A similar procedure is employed in the third direction for three-dimensional cases.

The second sub-step requires the solution of the pressure correction equation

$$\frac{u_i^{n+1} - u_i^*}{\Delta t} = -\frac{1}{\rho}\frac{\delta p'}{\delta x_i}, \tag{2.4}$$

which is solved with the constraint that the final velocity u_i^{n+1} be divergence-free. This gives the following Poisson equation for the pressure correction

$$\frac{1}{\rho}\frac{\delta}{\delta x_i}\left(\frac{\delta p'}{\delta x_i}\right) = \frac{1}{\Delta t}\frac{\delta U_i^*}{\delta x_i} \tag{2.5}$$

and a Neumann boundary condition imposed on this pressure correction at all boundaries. This Poisson equation is solved with a highly efficient geometric multigrid method which employs a line based Gauss–Siedel successive over-relaxation (SOR) smoother. Once the pressure correction is obtained, the pressure and velocity are updated as

$$p^{n+1} = p^n + p', \tag{2.6a}$$

$$u_i^{n+1} = u_i^* - \Delta t \frac{1}{\rho}\left(\frac{\delta p'}{\delta x_i}\right)_{cc}, \tag{2.6b}$$

$$U_i^{n+1} = U_i^* - \Delta t \frac{1}{\rho}\left(\frac{\delta p'}{\delta x_i}\right)_{fc}, \tag{2.6c}$$

These separately updated face velocities satisfy discrete mass-conservation to machine accuracy and use of these velocities in estimating the nonlinear convective flux in (2.2) leads to a more accurate and robust solution procedure. The procedure of separately computing the face-centre velocities was initially proposed by Zang, Street & Koseff (1994) and discussed in the context of the Cartesian grid methods in Ye *et al.* (1999).

2.2. *Immersed boundary treatment*

A multi-dimensional ghost-cell methodology is used to incorporate the effect of the immersed boundary on the flow. This method falls into the category of sharp-interface 'discrete forcing' immersed boundary methods (Mittal & Iaccarino 2005). Figure 2 shows a two-dimensional schematic of an immersed boundary on a Cartesian grid. The surface of three-dimensional bodies such as the ellipsoids that are the subject of the current study, is represented by an unstructured grid with triangular elements. A typical surface grid for a (1 : 0.12 : 4) ellipsoid is shown in figure 3. This surface grid is then 'immersed' into the Cartesian volume grid. The method proceeds by identifying 'ghost-cells' which are cells inside the solid that have at least one neighbour in the fluid. A 'probe' is then extended from the node of these cells into the fluid to an 'image-point' (denoted by IP) such that it intersects normal to the immersed boundary and the boundary intercept (denoted by BI) is midway between the ghost-node and the image-point. Next a bilinear (trilinear in three-dimensions) interpolation is used to express the value of a generic variable (say ϕ) at the image-point in terms of the surrounding nodes, namely,

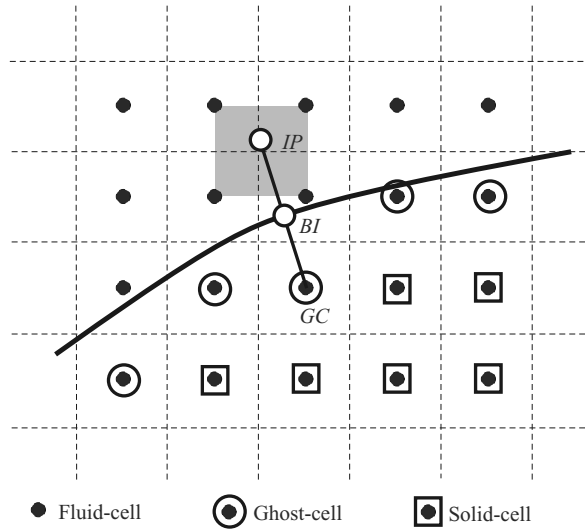$$\phi_{IP} = \sum \beta_i \phi_i. \tag{2.7}$$

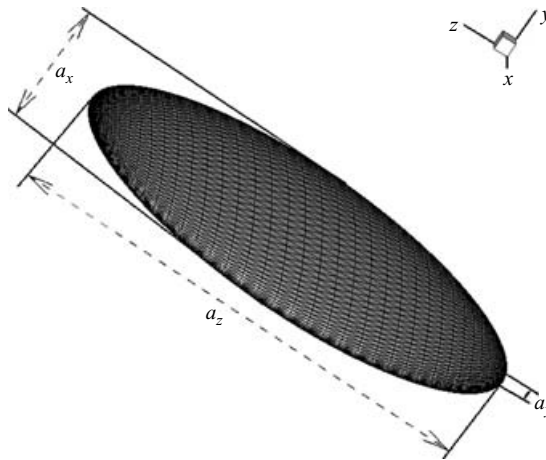FIGURE 2. Schematic describing ghost-cell methodology.

FIGURE 3. Typical ellipsoidal foil used in the current study. The surface of the ellipsoid is represented by an unstructured grid made of triangular elements.

where i extends over all the surrounding nodal points and β_i are the interpolation weights corresponding to the nodes surrounding the image-point. Note that all of the information regarding the local geometry of the boundary and its placement relative to the grid is incorporated solely in these weights. Following this, the value of a variable at the ghost-cell (denoted by GC) is computed by using a central-difference approximation along the normal probe such that the prescribed boundary condition at the boundary intercept is incorporated. Thus, for Dirichlet and Neumann boundary conditions, the formulae are:

$$\phi_{GC} = 2\phi_{BI} - \phi_{IP}, \qquad (2.8a)$$

$$\text{and } \phi_{GC} = \Delta l_p \left(\frac{\delta \phi}{\delta n} \right)_{BI} + \phi_{IP}, \qquad (2.8b)$$

respectively, where Δl_p is the total length of the probe. Equations (2.7) and (2.8) can be combined to give the following implicit expression for the values at the ghost nodes:

$$\phi_{GC} + \sum \beta_i \phi_i = 2\phi_{BI}, \tag{2.9a}$$

$$\phi_{GC} - \sum \beta_i \phi_i = \Delta l_p \left(\frac{\delta \phi}{\delta n} \right)_{BI}, \tag{2.9b}$$

respectively, for these two types of boundary condition. These equations are then solved in a fully coupled manner with the discretized governing equations (2.2) and (2.5) for the neighbouring fluid cells along with the trivial equation $\phi = 0$ for the internal solid cells. Using this procedure, the boundary conditions are prescribed to second-order accuracy and this, along with the second-order accurate discretization of the fluid cells leads to local and global second-order accuracy in the computations. This has been confirmed by simulating flow past a circular cylinder on a hierarchy of grids and examining the error on these grids (Bozkurttas *et al.* 2005).

Boundary motion can now be included into this formulation with relative ease. Since the equations are written in the Eulerian form, all that is required is to move the boundary at a given time-step, recompute the body-intercepts, image-points and associated weights β and then advance the flow equations (2.2)–(2.6c) in time. The boundary motion is accomplished by moving the nodes of the surface triangles in a prescribed manner. The general framework can therefore be considered as Eulerian–Lagrangian, wherein the immersed boundaries are explicitly tracked as surfaces in a Lagrangian mode, while the flow computations are performed on a fixed Eulerian grid. Further details regarding such immersed boundary methods can be found in Ye *et al.* (1999), Udaykumar *et al.* (2001) and Mittal & Iaccarino (2005). In addition to the simulations to be presented here, the solver has been used successfully in a CFD validation study involving transitional synthetic-jets (Kotapati & Mittal 2005) and has also been validated by simulating flow past a suddenly accelerated normal plate and comparing results with available experiments and simulations (Bozkurttas *et al.* 2005).

2.3. *Simulation set-up*

The current study employs thin ellipsoidal foils of varying aspect ratio in all the simulations. The geometry of the foil is defined by its three major axes denoted by a_x, a_y and a_z (figure 3). Note that we employ the (x, y, z)-axes notation in the rest of the paper. In the current simulations, the surface of the foil is represented by a fine unstructured grid with triangular elements and the foil is oriented with the x-axis along the streamwise direction and the z-axis along the spanwise direction. Furthermore, a_x is the chord of the foil which in these simulations is set equal to unity and a_y is the foil thickness. The thickness ratio a_y/a_x for all the foils in the current study is equal to 0.12. The aspect ratio $Æ$ of the foil is defined as (span)^2/(area) which is equal to $(4/\pi)a_z/a_x$ for these ellipsoidal foils. In the current study, in addition to a two-dimensional flapping foil for which $Æ = \infty$, we examine a foil with $a_z/a_x = 1$ ($Æ = 1.27$) which corresponds to a circular disk, and two ellipsoidal foils with $a_z/a_x = 2$ ($Æ = 2.55$) and 4 ($Æ = 5.09$).

The foil undergoes a combined pitching and heaving motion wherein the foil centre heaves in the y-direction according to

$$y(t) = A_y \sin(2\pi f t), \tag{2.10}$$

$A\!R$	a_y/a_x	Re	St	A_y/a_x	θ_0	A_θ
1.27, 2.55, 5.09, ∞	0.12	100, 200, 400	0.3, 0.4, 0.5, 0.6, 0.7, 0.8, 1.0, 1.2	0.5	0°, 10°, 20°, 30°	30°

TABLE 1. Parameters involved and ranges of variation in the current study.

and pitches about the centre according to

$$\theta(t) = \theta_0 + A_\theta \cos(2\pi f t), \tag{2.11}$$

where θ is the geometric pitch-angle with respect to incoming flow. In (2.10) and (2.11) θ_0 is the pitch-bias angle, A_y and A_θ are the heave and pitch amplitudes, respectively, and f is the flapping frequency. Note that the pitch angle variation is phase advanced by 90° with respect to the heave motion. Other values of phase-difference between heaving and pitching have been examined by Isogai *et al.* (1999), Tuncer, Walz & Platzer (1998) and Ramamurti & Sandberg (2001) among others.

In addition to the foil aspect ratio ($A\!R$), the following are the key non-dimensional parameters in the current study: Reynolds number $Re = U_\infty a_x/\nu$; normalized heave amplitude A_y/a_x, pitch-bias angle θ_0, pitch amplitude A_θ and Strouhal number based on the wake thickness $St = 2A_y f/U_\infty$. It is clear that even this relatively simple configuration has a very high dimensional parameter space. With regard to A_y/a_x, it should also be pointed out that in fish that flap their pectoral fins, the flapping amplitude can vary over a relatively large range depending on the fish as well as its speed of travel (Lauder *et al.* 2005; Walker & Westneat 2002). However, in order to limit the scope of this study, we choose to fix the normalized heave amplitude A_y/a_x to a value of 0.5 and the pitch amplitude A_θ to a value of 30°. Similar values have been adopted in a number of past studies (von Ellenrieder *et al.* 2003; Lewin & Haj-Hariri 2003; Triantafyllou, Techet & Hover 2004) and the amplitude adopted is for instance, a reasonable representation of the mid-span kinematics of the bluegill sunfish pectoral fin kinematics (Lauder *et al.* 2005). Table 1 provides a concise summary of all the parameters involved and their range of variation.

The grids employed in the current study are designed to provide high resolution in the region around the flapping foils as well as in the wake region and figure 4 shows two two-dimensional sections of a typical grid in the (x, y)- and (x, z)-planes. A relatively large domain size is chosen and the foil is placed approximately at the centre of this domain. At the left-hand boundary, we provide a constant inflow velocity boundary condition, and a zero stress boundary condition is provided at all the lateral boundaries. The right-hand boundary is the outflow boundary and there we provide a zero streamwise gradient boundary condition for velocity which allows vortices to convect out of this boundary without significant reflections. A homogeneous Neumann boundary condition is used for pressure at all these boundaries.

In the current study, the thrust, lift and moment coefficients are defined as

$$C_T = \frac{T}{\frac{1}{2}\rho U_\infty^2 A_{plan}}, \quad C_L = \frac{L}{\frac{1}{2}\rho U_\infty^2 A_{plan}}, \quad C_M = \frac{M}{\frac{1}{2}\rho U_\infty^2 A_{plan} a_x}, \tag{2.12}$$

respectively, where T, L and M are the thrust, lift and pitching moments, respectively, and A_{plan}, the planform projected area of the foil, is equal to $\pi a_x a_z/4$ for the ellipsoidal foils and a_x for the two-dimensional foil. Thrust is calculated by directly integrating
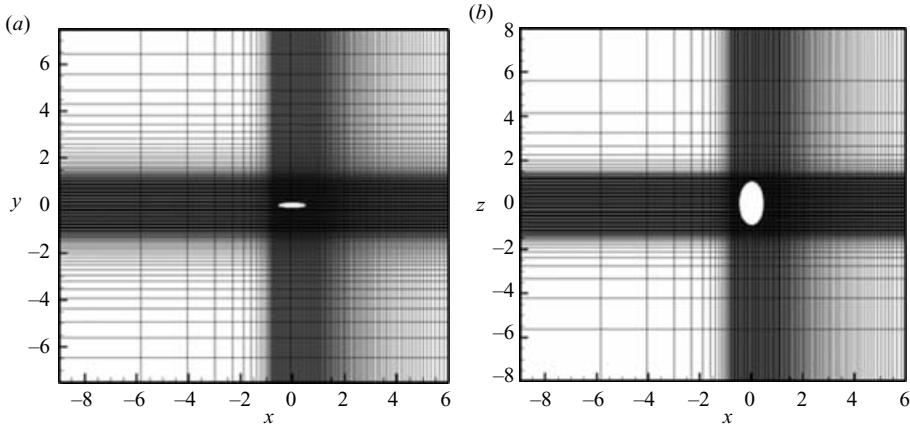
FIGURE 4. Typical grid employed in the current simulations for the lower-aspect-ratio foils. This grid is $145 \times 129 \times 101$ and the domain size is $15 \times 15 \times 16$. (*a*) (x, y)-view (*b*) (x, z)-view.

the computed pressure and shear stress on the foil surface. In all cases, the governing equations are advanced in time until the force coefficients indicate that the flow has reached a stationary state. Following that, the simulation is run further for a number of cycles and data from these later cycles are used in the analysis as well as for computing the flow statistics. We also compute a propulsive efficiency which is given by

$$\eta = \frac{\overline{T} U_\infty}{\overline{L \mathrm{d}y/\mathrm{d}t + M \mathrm{d}\theta/\mathrm{d}t}},$$
(2.13)

where the overbar implies a time average. The typical time step chosen in the current study was such that there were over two thousand time steps in each cycle, thereby ensuring more than adequate temporal accuracy.

2.4. *Grid and domain independence studies*

The nominal grid size employed in the current simulations is $144(x) \times 128(y) \times 104(z)$ which amounts to about 1.92 million grid points. Domain sizes range from $15a_x(x) \times 15a_x(y) \times 16a_x(z)$ for the small-aspect-ratio foils to $15 \times 15 \times 32$ for the large-aspect-ratio ($A\!R = 5.09$) foil. This choice of grid and domain size was based on our experience with the simulations of such flows as well as running test simulations on a number of different grids. Figure 4 shows two views of a typical grid used in the current study. As can be seen in this figure, very high resolution is provided in a cuboidal region around the foil in all three directions. Beyond this region, the grid is stretched rapidly in the y- and z-directions. In the x-direction, the stretching is rapid upstream of the foil where we do not expect any streamwise gradient. In the wake region, however, the stretching factor is kept below 3 % in order to keep the streamwise resolution relatively high. This also limits the numerical dispersion that is associated with the use of central-difference schemes on highly stretched meshes (Cain & Bush 1994). Both of these factors are important in order to ensure adequate resolution of the fine structures in the wake.

Comprehensive studies have been carried out to assess the effect of the grid resolution and domain size on the salient features of the computed flow and to demonstrate that the chosen grids produce accurate results. Grid refinement studies are carried out by doubling the grid in all three directions simultaneously in the refined

Case	$\overline{C}_T$	$(C_L)_{rms}$	η
Nominal grid	0.246	1.780	0.1846
Finer grid	0.248	1.816	0.1851
Larger domain	0.246	1.798	0.1849

TABLE 2. Results of grid refinement and domain independence study for $A\!R = 2.55$, $St = 0.6$ and $Re = 200$ case.

zone around the foil. Beyond this region the resolution is increased nominally in order to ensure a smooth grid. The overall grid size for this refined grid is $192 \times 176 \times 144$ which amounts to about 4.87 million grid points. Domain independence studies are carried out by doubling the domain size in all three directions to $30 \times 30 \times 32$. In this study, the resolution in the interior refined region is kept the same as the nominal grid, but the resolution in the outer region is increased so as to maintain the same stretching ratio as the nominal grid. The overall grid size for this domain is $160 \times 144 \times 136$ which amounts to 3.13 million mesh points. All these simulations have been carried out on a single processor computer with a 64-bit AMD Opteron processor with 8 Gb of core memory. Each nominal grid simulation takes anywhere from 200 to 400 CPU hours on this computer.

Table 2 shows a comparison of key hydrodynamic quantities for the grid and domain independence study carried out for the $A\!R = 2.55$, $St = 0.6$ and $Re = 200$ case. The table shows that the grid refinement and domain enlargement lead to less than 1% difference in the mean thrust and efficiency and at most about 2% variation in the r.m.s. lift. This clearly demonstrates that the hydrodynamic forces computed in the current study are grid and domain independent. In addition to the above comparison of the hydrodynamic forces and moments, it is useful to assess the effect of the grid and domain on the flow development in the wake. In figure 5, we compare the wake profiles for these three different grids. Figures 5(*a*) and 5(*b*) show the mean streamwise $(\overline{u}_1 - U_\infty)$ and transverse $(\overline{u}_2)$ velocity profiles in the spanwise symmetry plane and figure 5(*c*) shows the spanwise mean velocity profiles in the centre (x, z)-plane. In all of these plots, we note that the differences between the profiles computed on the three different grids are negligible. Also plotted in figure 5(*d*) are profiles of the fluctuation kinetic energy defined as $\frac{1}{2}(\overline{u_1'^2} + \overline{u_2'^2} + \overline{u_3'^2})$ in the spanwise symmetry plane. Comparison of these profiles is an even more severe test of grid dependence since the fluctuations inherently contain more information from the smaller spatial and temporal scales in the flow. Here too we find that the difference between the three sets of profiles is small, and this clearly establishes the fidelity and accuracy of the current simulations.

3. Results

In this section, we provide a comprehensive description of the wake topology followed by a discussion of the thrust performance of these flapping foils for the range of parameters shown in table 1.

3.1. *Wake topology*

The focus in this section is to describe the effect of aspect ratio on the vortex topology. Vortices in three-dimensional simulations are identified by plotting an isosurface of the imaginary part of the complex eigenvalue of the instantaneous velocity gradient tensor.
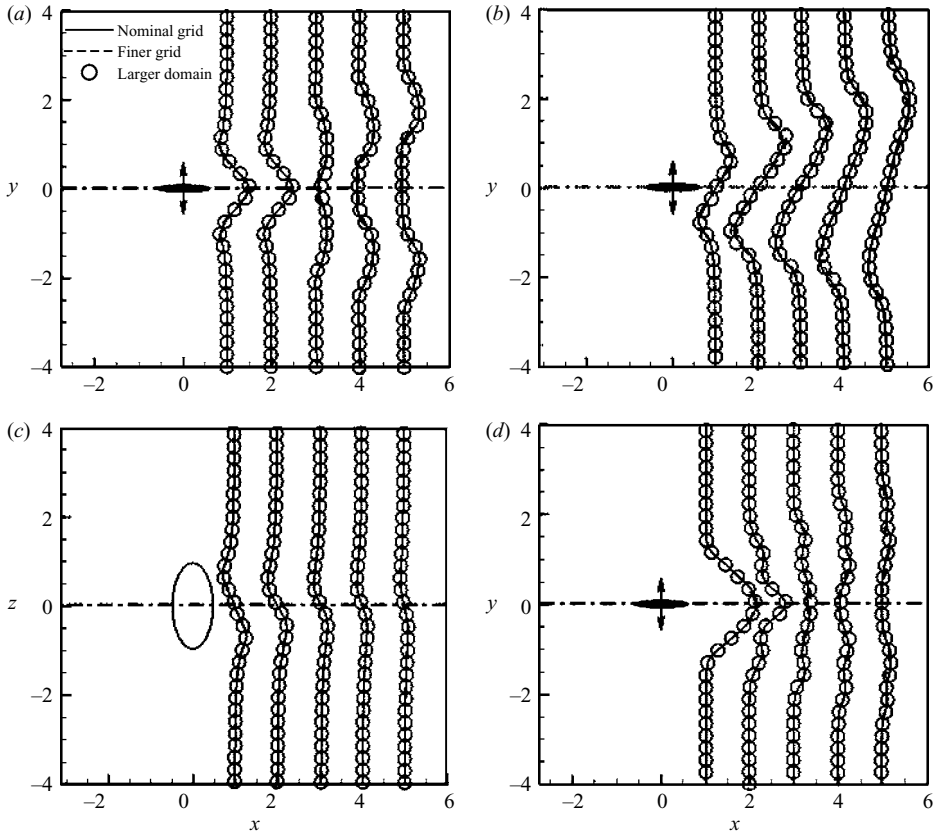
FIGURE 5. Comparison of computed profiles in the wake showing grid and domain independence of computed results for the $AR = 2.55$, $St = 0.6$ and $Re = 200$ case. Five profiles at $x = 1, 2, 3, 4$ and 5 are shown. (a) Streamwise ($\bar{u}_1 - U_\infty$) velocity on the spanwise symmetry plane, (b) transverse ($\bar{u}_2$) velocity on the spanwise symmetry plane, (c) spanwise ($\bar{u}_3$) velocity on the transverse symmetry plane, (d) fluctuation kinetic energy $\frac{1}{2}(\overline{u_1'^2} + \overline{u_2'^2} + \overline{u_3'^2})$ on the spanwise symmetry plane.

This approach for identifying vortices in 3D flow fields has been advocated by Soria & Cantwell (1993) and has been used extensively for extracting the vortex topology in cylinder (Mittal & Balachandar 1995) and sphere wakes (Mittal, Wilson & Najjar 2002b). The idea behind this technique is to identify regions where rotation dominates over strain. Since the rotational part of the velocity gradient tensor is skew-symmetric, it is likely that in these regions, the eigenvalue of the velocity gradient tensor will have a relatively large imaginary component. Therefore the magnitude of the imaginary component of the eigenvalue of the velocity gradient tensor provides a means of identifying vortices in the flow.

In §§ 3.1.1–3.1.4, we describe the effect of aspect ratio on the vortex topology and wake structure for flapping foils without pitch-bias. For this analysis, we focus on cases with $Re = 200$ and $St = 0.6$, which are roughly in the middle of the range for these parameters in the current study. The effect of the Strouhal and Reynolds numbers as well as pitch-bias is examined in subsequent sections. In describing the effect of aspect ratio on the vortex topology, we proceed as follows: we first describe the $AR = \infty$ case which is two-dimensional and serves as the baseline for the finite-aspect-ratio cases.
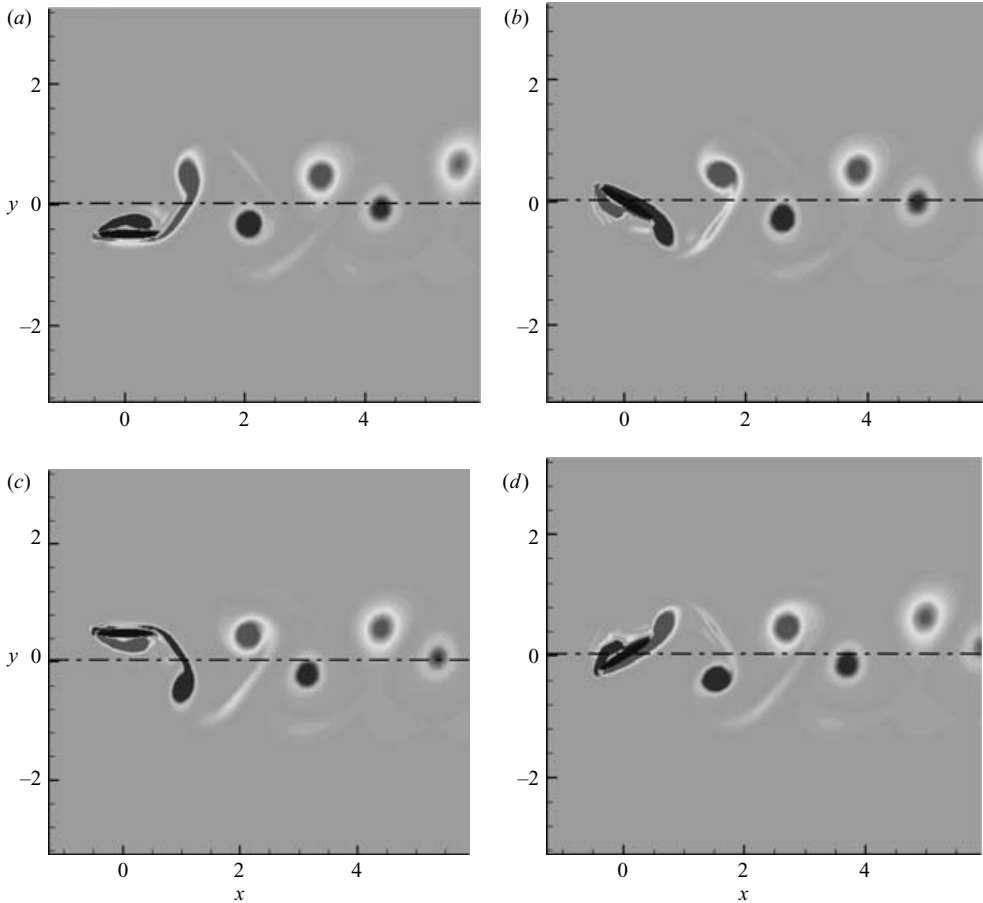
FIGURE 6. Vortex topology for $\mathcal{R} = \infty$ foil at four phases visualized by plotting contours of spanwise vorticity. There are 35 equispaced contour levels of non-dimensional spanwise vorticity ranging from -9 to 9 in this and all other spanwise vorticity contour plots in the current paper. (*a*) $ft = 0$, (*b*) $ft = 1/4$, (*c*) $ft = 1/2$, (*d*) $ft = 3/4$.

Subsequently, we describe the $\mathcal{R} = 2.55$ case, which is the intermediate finite-aspect-ratio case in the current study as well as the case which is most relevant to fish pectoral-fins. This is followed by a description of the $\mathcal{R} = 1.27$ and 5.09 cases.

3.1.1. $\mathcal{R} = \infty$ case

This infinite-aspect-ratio foil has been simulated as two-dimensional. This foil is thrust producing with its mean thrust coefficient being 0.91. Figure 6 shows a sequence of spanwise vorticity contour plots at four instances in the flapping cycle and these plots clearly show the formation of an inverse Kármán vortex street. The appearance of this vortex topology for this thrust-producing flapping foil is consistent with Koochesfahani (1989), Triantafyllou *et al.* (1992) and Lewin & Haj-Hariri (2003). Figure 7 shows contours of the mean streamwise velocity where the mean is computed over five shedding cycles. The plot shows a narrow high-intensity jet in the wake which is consistent with the fact that this is a thrust-producing case. Also apparent is the asymmetry of this jet about the centreline. This asymmetry is consistent with the finding of Jones *et al.* (1998) and Lewin & Haj-Hariri (2003) where asymmetric wakes
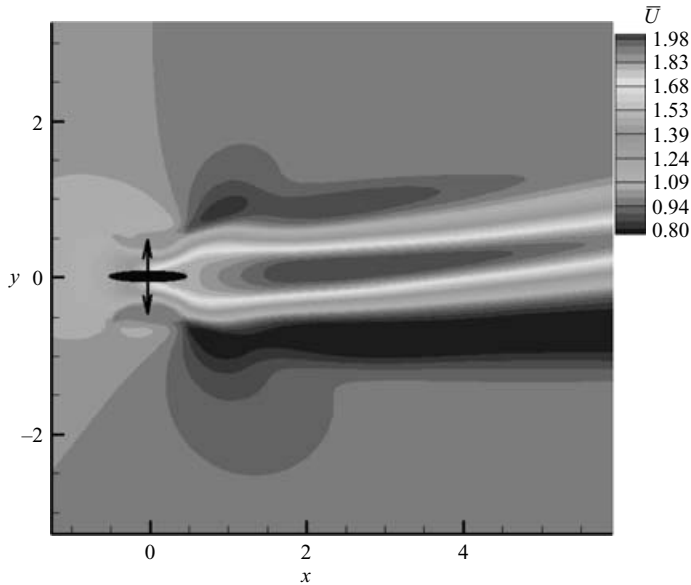
FIGURE 7. Contours of mean streamwise velocity for the $\mathcal{R} = \infty$ case. The plot shows a narrow high-velocity jet which is asymmetric about the centreline.

have been observed for a thrust-producing flapping foil. Although Jones *et al.* (1998) have examined the flow associated with sinusoidally heaving foils whereas Lewin & Haj-Hariri (2003) have studied foils undergoing a combined pitch-and-heave, both studies find that for values of $\pi St > 1$, the wake appears asymmetric or 'deflected'. The value of this parameter for the current simulation is 1.88 and therefore asymmetry in the current flow is very much in-line with these previous findings. The direction of the wake deflection is determined by the starting motion of the foil. In the current study, the foil starts at its bottom-most location and moves up initially and this produces a wake with an upward deflection. If the foil is started at the uppermost point and moved down, a downward deflection is obtained. However, once deflected towards one side of the centreline, the wake does not switch sides in a given simulation. The asymmetry produces a mean transverse force that is significantly lower in magnitude than the mean thrust force and therefore has little dynamical significance.

3.1.2. $\mathcal{R} = 2.55$ *case*

In this section, we examine the wake topology for the $\mathcal{R} = 2.55$ flapping foil. Figures 8(*a*) and 8(*b*) show perspective and side views of the vortex topology for this case at a phase when the foil is at the lowest point in its heaving cycle. Also, shown in figure 8(*d*) is a contour plot of the spanwise vorticity at the spanwise symmetry plane at this phase allowing for a direct comparison with the $\mathcal{R} = \infty$ case. In all these plots, distinct vortices have been identified and named so as to facilitate discussion regarding their evolution. It is also important to point out that similar to the two-dimensional foil, this is a thrust-producing foil with a mean thrust coefficient $\overline{C}_T = 0.246$.

Comparison of figure 8(*d*) with the corresponding plot for the $\mathcal{R} = \infty$ case (in figure 6) shows some common features including the presence of the clockwise vortex V_1 in the wake, the counterclockwise vortex V_2 shedding from the trailing-edge and the clockwise leading-edge vortex V_3 on the top surface of the foil. However,
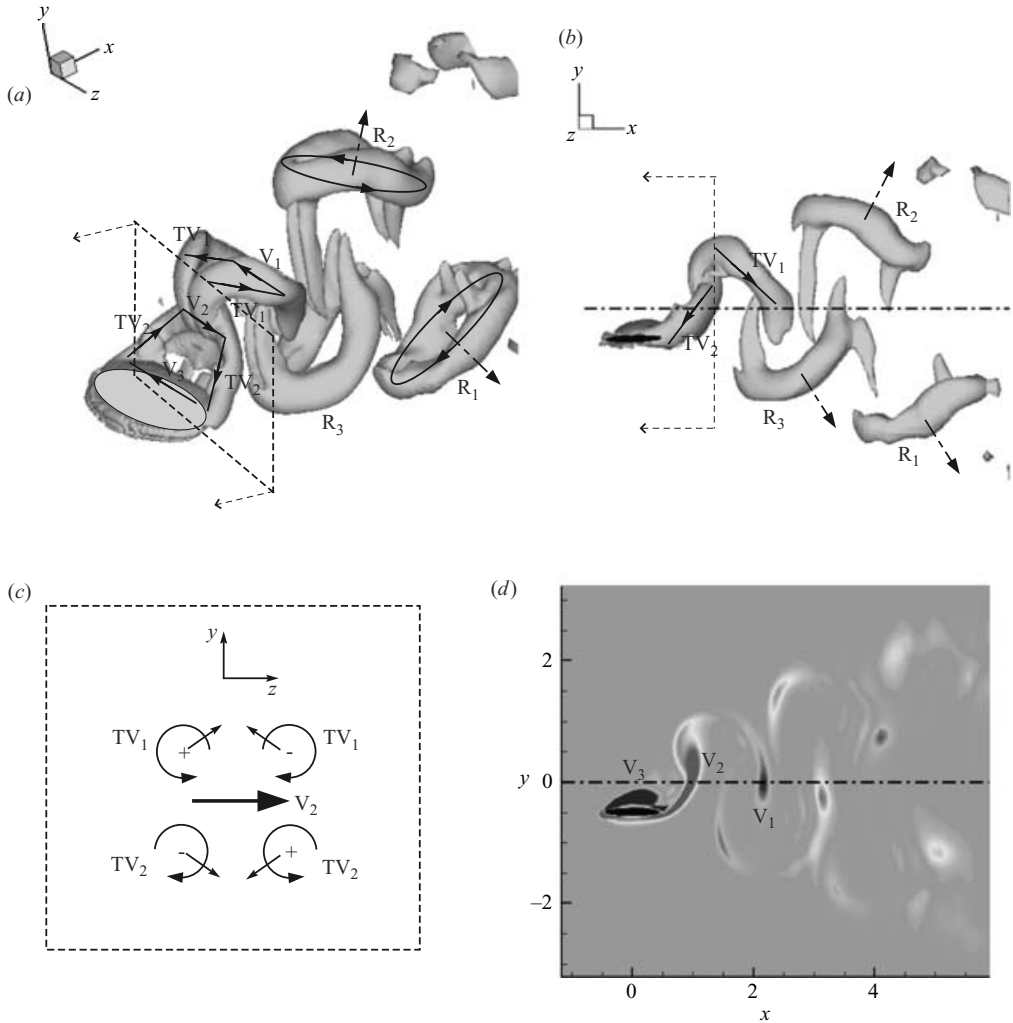
FIGURE 8. Vortex topology for $R = 2.55$ foil at the phase where the foil is at the lowest point in its heaving motion and starting to move up. This and all other three-dimensional vortex topology plots are visualized by plotting one isosurface of the imaginary part of the complex eigenvalue of the velocity gradient tensor corresponding to a value of 1.0. (*a*) Perspective view. (*b*) Side view. (*c*) Front-view schematic of tip vortices on streamwise plane indicated in (*a*) and (*b*). (*d*) Spanwise vorticity contour plot on spanwise symmetry plane.

notwithstanding these similarities, we also see significant differences emerge between the two wakes with the most striking difference being the complete disappearance of the inverse Karman vortex street in the $R = 2.55$ flapping foil. Explanation of this fundamental change in the wake structure requires us to consider the three-dimensional topology of the wake. It is clear from the three-dimensional perspective view of the wake topology in figure 8(*a*) that the wake of this foil in fact, has little resemblance to the two-dimensional foil case. This plot as well as the side view in figure 8(*b*) shows that the downstream wake of this foil consists of two sets of complex shaped vortex rings which convect at oblique angles to the wake centreline. In the plots, we identify rings R_1 and R_3 in the lower set and R_2 in the upper set

and indicate their direction of rotation by lines and arrows. It is also noted that each vortex ring has two sets of thin vortex 'contrails' (see for instance ring R_2 in figure 8b) at its upstream and downstream ends that extend towards the two adjacent counter-rotating rings. As the vortices convect downstream, these contrails become weaker and ultimately disappear (as for ring R_1) leaving fairly well-defined vortex rings. The vortex rings are themselves inclined with respect to the free stream (as shown by the ring-axes arrows in figure 8b). Thus, the flow induced by each vortex ring along its axis is expected to have a net streamwise component with the cross-stream component of vortex rings in one set being offset by those in the other. As will be shown later, this net streamwise momentum excess in the wake is also connected with the thrust production of the flapping foil.

The process by which the rings are formed and the particular orientation and shape adopted by them can be explained by examining the vortex formation and shedding process closer to the foil trailing edge. In figures 8(a) and 8(b) consider vortex V_2 as well as its two associated tip-vortices identified as TV_2 which constitute the three sides of a vortex loop. Note that vortex V_2 is associated with the trailing-edge vortex that is released from the lower surface of the foil as it moves downward whereas the tip-vortices are released from the spanwise tips of the flapping foil in a similar manner. Vortex V_3 which is formed at the leading-edge due to the downward motion, is shown disconnected from this vortex loop and the reasoning behind this will soon become clear. Now it is straightforward to understand that the vortex loop associated with vortex V_1 and tip vortices TV_1 was formed in the previous half-cycle in a similar manner. It remains to be explained how these vortex loops turn into vortex rings further downstream and why they convect at an angle oblique to the wake centreline.

Regarding ring formation, it would seem that the obvious mechanism, if we were to consider the loop consisting of V_1 and TV_1, is that vortex V_2 joins with TV_1 thereby forming a ring which then convects downstream. However, closer examination indicates that this is not the case here. Instead as shown in figures 9(a), 9(c) and 9(d) which correspond to a later phase when the foil is midway and moving up, vortex V_2 does not join with V_1 and TV_1 and the completion of the ring occurs primarily due to the the joining of the two tip-vortices TV_1 which leads to the formation of a spanwise structure V_{12} as shown in these plots. The process by which the upstream ends of the tip vortices TV_1 move towards each other can be understood by examining flow in the streamwise plane in this region as indicated in figures 8(a) and 8(b) by the dashed line. A schematic of the tip-vortices TV_1 and TV_2 and spanwise vortex V_2 on this plane is shown in figure 8(c). The direction of the velocity induced on one tip-vortex by the other three is represented by the arrow and this clearly shows that the vortices in the same system will tend to move towards each other. This deformation of the vortices TV_1 eventually leads to the formation of the spanwise oriented vortex V_{12} which completes the vortex ring. Thus, vortex V_2 does not join with vortices V_1 and TV_1 to form the vortex ring. In fact, the schematic also indicates that the tip-vortices compress the spanwise vortex V_2 and this tends to diminish the strength of the spanwise vortices as they convect downstream.

Figure 8(c) also indicates that the tip-vortices in one loop will tend to move away from the tip-vortices of the adjoining loop. This is very apparent by comparing figures 8(d) and figures 9(d) where we see that the incipient vortex V_{12} visible in figure 8(d) just above but joined with vortex V_2, achieves significant vertical separation from vortex V_2 by the time the foil gets to the centre. This tip-vortex-induced upward motion of vortex V_1 is the primary mechanism that leads to the inclination of the vortex ring. Once the ring is inclined, its self-induced velocity tends
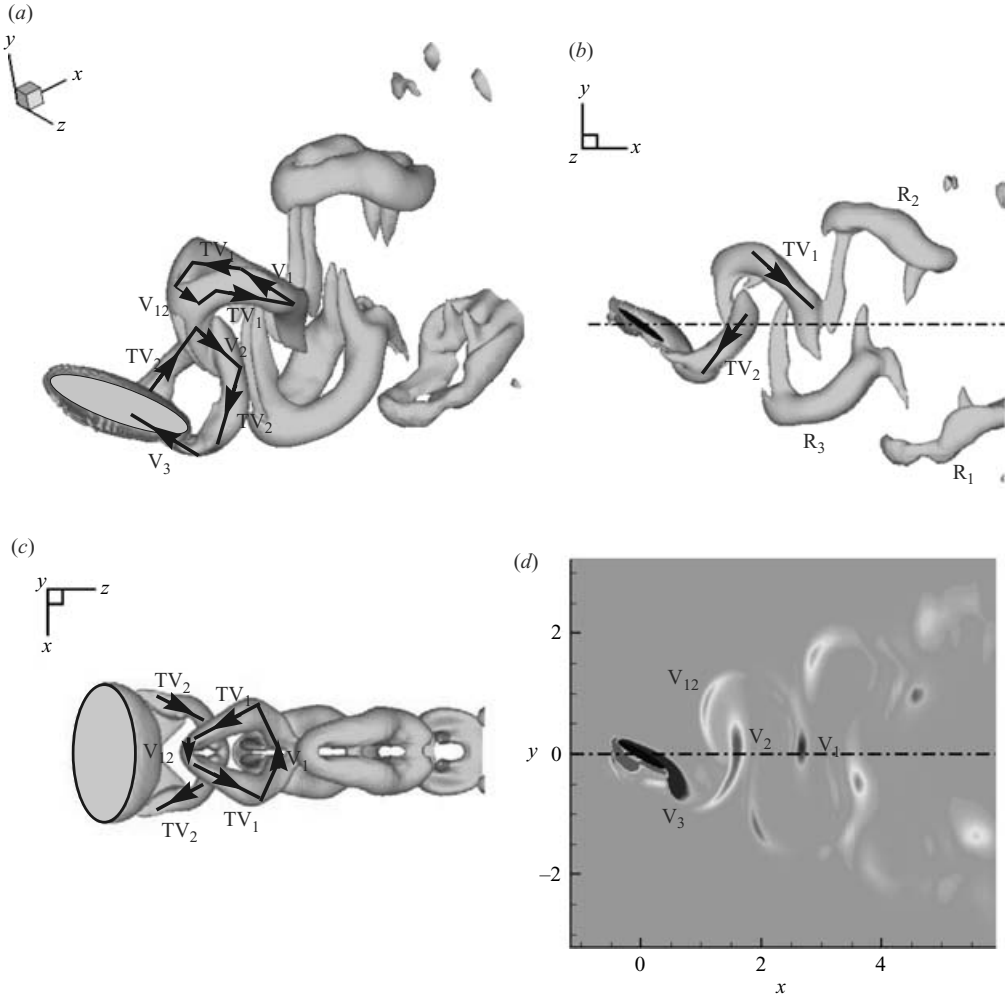
FIGURE 9. Vortex topology for $\mathcal{R} = 2.55$ foil at the phase where the foil is at the centre of its heaving motion. (*a*) Perspective view. (*b*) Side view. (*c*) Top view. (*d*) Spanwise vorticity contour plot on spanwise symmetry plane.

to convect it along its axis and this mechanism then explains the convection of the vortex rings at an oblique angle to the wake centreline. The experimental visualizations of Buckholtz & Smits (2006) for a pitching panel also show a bifurcation in the wake very similar to what is seen here. It should also be pointed out that in figure 9(*c*) which is a top-view, we see a spanwise narrowing of the vortex rings as they convect downstream. This is clearly due to the induction of one set of tip-vortices on the adjacent set as explained in the previous paragraph. Spanwise narrowing has also been observed in the simulations of Blondeaux *et al.* (2005*a*, *b*) for a rectangular pitching–heaving foil as well as the experiments of Buckholtz & Smits (2006) for a pitching plate. In contrast, the experiments of von Ellenrieder *et al.* (2003) do not show any clear spanwise narrowing and the reason for this disagreement is not clear. Also in agreement with Blondeaux *et al.* (2005*a*, *b*) and Buckholtz & Smits (2006), we do not observe a distinct vortex loop associated with the trailing-edge as was observed by von Ellenrieder *et al.* (2003).
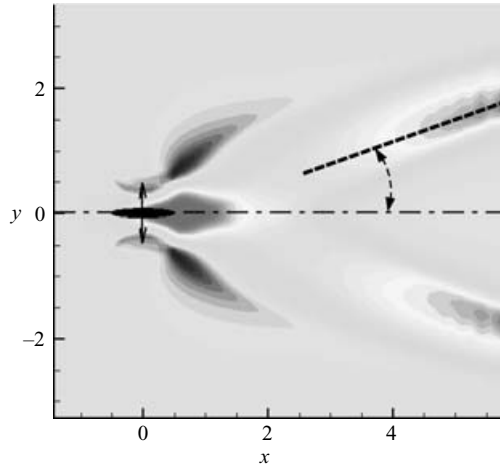
FIGURE 10. Contours of mean streamwise velocity for the $\mathcal{R} = 2.55$ case along the spanwise symmetry plan. Contour levels in this plot are the same as those in figure 7.

The last distinct feature that requires explanation is the vortex contrails that are seen extending from the upstream end of one loop to the downstream end of the previous loop. If we consider the ones extending from vortex V_{12} to vortex V_2 in figure 9(a), it is clear that these structures are segments of the tip-vortices TV_1 which are induced by the V_2 vortex to wrap around itself in a counterclockwise direction.

Figure 10 presents contours of the mean streamwise velocity along the spanwise symmetry plane for this case. From these plots, we observe that the wake develops a bifurcated jet with a relatively large inclination angle to the wake centreline. For this case, the inclination angle of each of the two branches of the wake from the symmetry line is about 16°. This angle is estimated by drawing a straight line through local maxima in mean streamwise velocity as indicated in figure 10. It is also worth pointing out that within statistical uncertainty, the mean wake is symmetric about the wake centreline. Thus, end effects tend to symmetrize the wake which is strongly asymmetric for the two-dimensional case at this Strouhal number. A closer examination shows that there is in fact a single streamwise directed jet in the very near wake which bifurcates about two chord-lengths downstream of the trailing edge. The inclination of the jet leads to a reduction in the streamwise momentum flux into the wake and this is connected with the lower thrust production of this finite-span flapping foil as compared to the two-dimensional foil.

The spanwise structure of these mean jets is examined by plotting contours of the mean velocity at several streamwise planes in figure 11. Figure 11(a) shows that the jet has a double-lobed structure in the near wake which clearly indicated that even in the very near wake, the influence of the tip vortices cannot be neglected. Further downstream at $x/a_x = 2$, we see in figure 11(b) the transverse bifurcation in the wake. In addition, each branch of the jet actually has two separate lobes and these lobes tend to merge further downstream (figure 11c). With regard to this merging it bears pointing out that the apparent intensification of the jets around $x/a_x = 6$ which is suggested by figure 10 is in fact not an intensification, but rather, a manifestation of the merging of the two lobes of the jet onto the spanwise symmetry plane.

The preceding discussion therefore explains the processes which lead to the formation of all the significant topological features in the wake of the finite-aspect-ratio
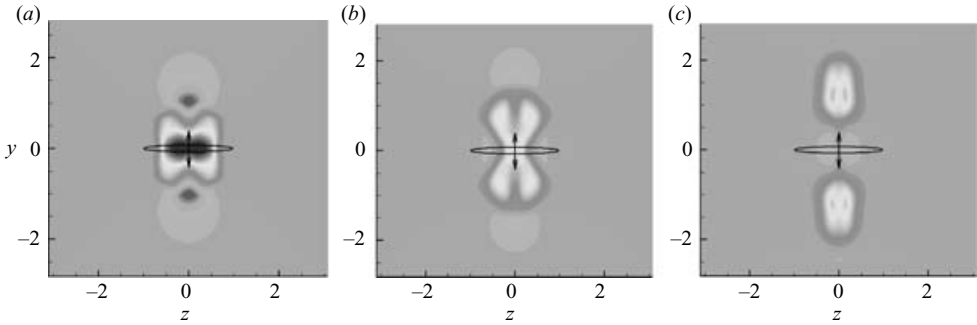
FIGURE 11. Contours of mean streamwise velocity for the $A\!R = 2.55$ case on three streamwise planes in the near wake (a) $x/a_x = 1$, (b) $x/a_x = 2$, (c) $x/a_x = 4$. Contour levels in this plot are the same as the ones in figure 7.

flapping foil. Using this discussion as the basis, we now examine the effect of aspect-ratio on the vortex topology.

3.1.3. $A\!R = 1.27$ case

Figures 12(a)–12(c) present three views of the 3D vortex topology for the foil with aspect ratio of 1.27, which is the lowest-aspect-ratio foil examined in the current study. This case is also thrust-producing with $\overline{C}_T = 0.073$. The wake for this foil shares a number of salient features with the $A\!R = 2.55$ foil wake. For instance, the plots show that the wake of this foil is also dominated by two sets of vortex rings. The side-view shows that these two sets of vortex rings convect at an oblique angle to the wake centreline. The rings in each set all have the same direction of rotation as indicated in the figure and their axis is also inclined with respect to the streamwise direction. The difference between this case and the previous case is mostly qualitative. First, the rings are more circular and this is obviously a consequence of the circular planform of the flapping foil. Secondly, the oblique angle is larger and this is because the ring axis is more vertical than in the previous case and this leads to a larger transverse induction velocity. This difference is most obvious when we compare the locations of vortices V_1 and V_{12} in figure 9(d) and figure 12(d). It can be seen that whereas in the previous case, vortex V_1 is located at the wake centreline at this phase, for the current case, vortex V_1 is significantly above the wake centreline.

The vortex arrangement on the spanwise symmetry plane in figure 12(d), can be viewed as two oblique inverse Kármán vortex streets, as indicated by the circular arrows in this figure. A similar arrangement can be seen for the $A\!R = 2.55$ flapping foil in figure 9(d). Thus, the inverse Kármán vortex street which is intimately linked with a two-dimensional thrust-producing flapping foil does seem to make an appearance even in small-aspect-ratio flapping foils.

Figure 13 presents contours of the mean streamwise velocity along the spanwise symmetry plane for this case. The plot shows that for this case also the wake develops a bifurcated shape at about one chord-length downstream of the trailing edge. The jet inclination angle for this case is about $20°$ which is larger than the $A\!R = 2.55$ case. This larger inclination angle is also a prognosticator of a further drop in thrust for this foil. Further, the mean wake is symmetric about the wake centreline. The spanwise structure of the mean wake is shown in figure 14. Figure 14(a) shows some indication of the four-lobed jet structure, but merger of the lobes in each jet further downstream results in a simpler wake structure, as with the previous case.
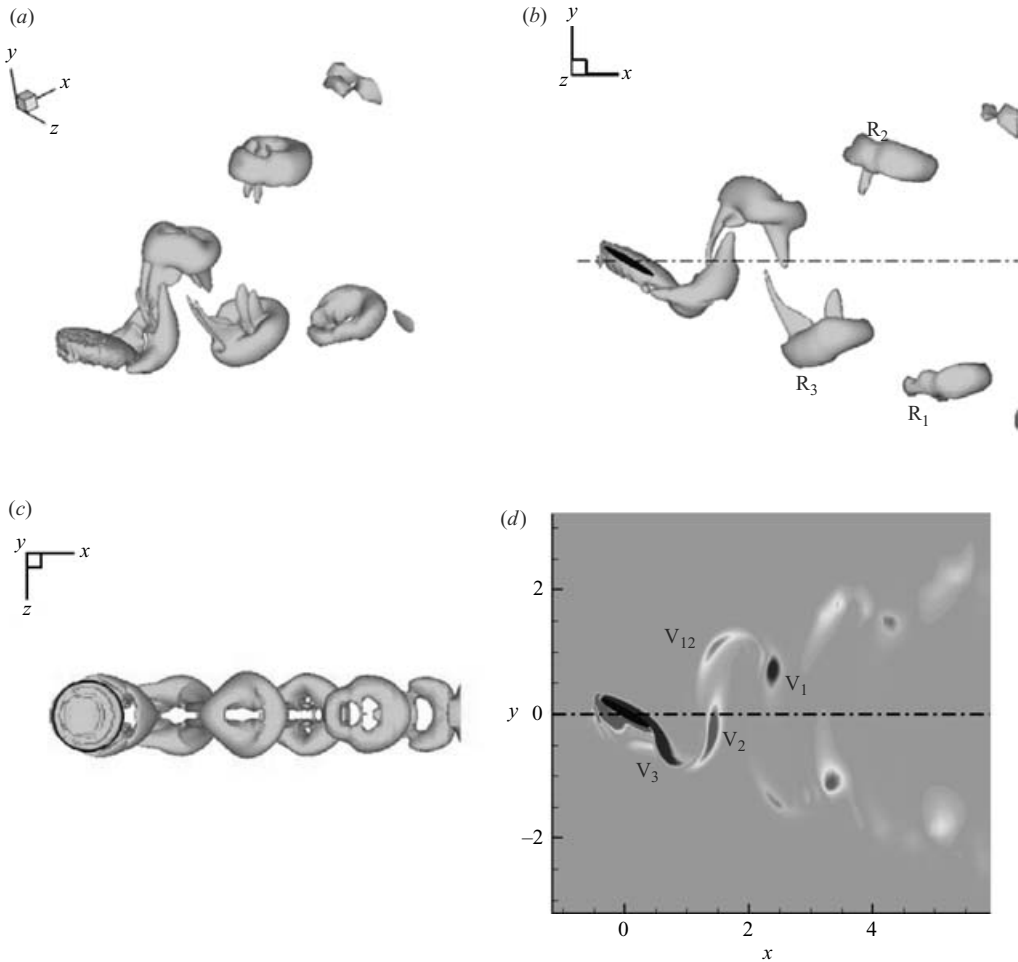
FIGURE 12. Vortex topology for $R = 1.27$ foil at phase where foil is at the centre of its heaving motion and moving up. (*a*) Perspective view. (*b*) Side view. (*c*) Top view. (*d*) Spanwise vorticity contour plot on spanwise symmetry plane.

3.1.4. $R = 5.09$ *case*

Finally, we consider the $R = 5.09$ foil, the largest finite-aspect-ratio foil considered in the current study and figure 15 shows the wake topology for this case. This large-aspect-ratio case enables us to connect our observations for the two-dimensional flapping foil with those for the lower-aspect-ratio flapping foils. The mean thrust coefficient for this case is 0.39 which is higher than the previous two cases, but lower than the two-dimensional case. Three key features differentiate this case from the lower aspect-ratio cases discussed in the previous sections. First, in this case, the tip-vortices are never seen to merge together and therefore no vortex rings are observed in the wake. Instead, the wake is made up of elongated loops that are seen to wrap end-on-end with adjacent loops. The absence of tip-vortex merging is simply because their initial distance is larger. It should be noted that associated with this observation is the absence of the secondary spanwise vortex V_{12} which was seen in the previous cases. The lack of ring formation also leads to the second key difference, which is the
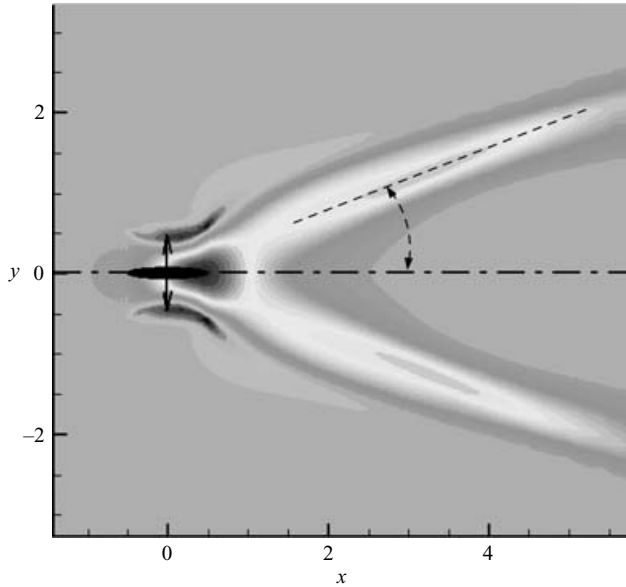
FIGURE 13. Contours of mean streamwise velocity for the $R = 1.27$ case along the spanwise symmetry plan. Contour levels in this plot are the same as those in figure 7.

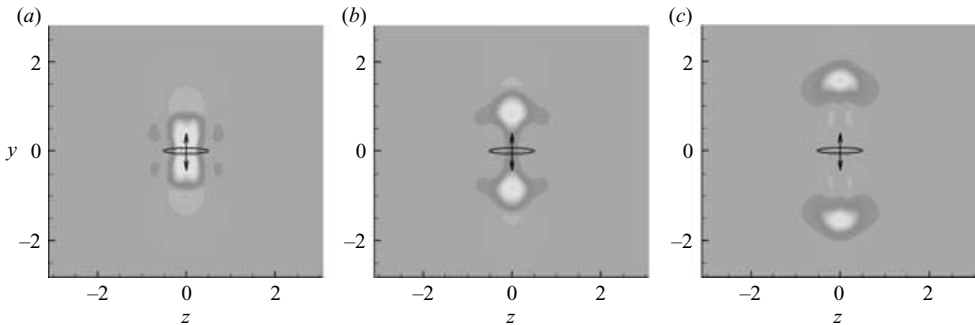FIGURE 14. Contours of mean streamwise velocity for the $R = 1.27$ case on three streamwise planes in the near wake (a) $x/a_x = 1$. (b) $x/a_x = 2$. (c) $x/a_x = 4$. Contour levels in this plot are the same as the ones in figure 7.

absence of two sets of obliquely convecting vortex structures. Instead, the two sets of vortex loops stay intertwined with each other. However, the wake itself expands rapidly in the transverse direction and this is clearly due to the self-induced velocity of the vortex loops. The third difference is the presence of distinctly spanwise oriented vortices in the very near wake such as vortex V_2 identified in figures 15(a) and 15(c). In fact, vortices V_1, V_2 and V_3 in figure 15(d) clearly signal the re-emergence of the conventional inverse Kármán vortex street seen in the wake of two-dimensional thrust-producing flapping foils. It should, however, be noted that further downstream, the spanwise vorticity diminishes in strength and the wake is dominated by the tip-vortices. This is primarily because while the spanwise vortices induce a stretching and therefore intensification of the tip-vortices, the tip-vortices induce a compression on the associated spanwise vortices which tends to diminish their strength. The spanwise
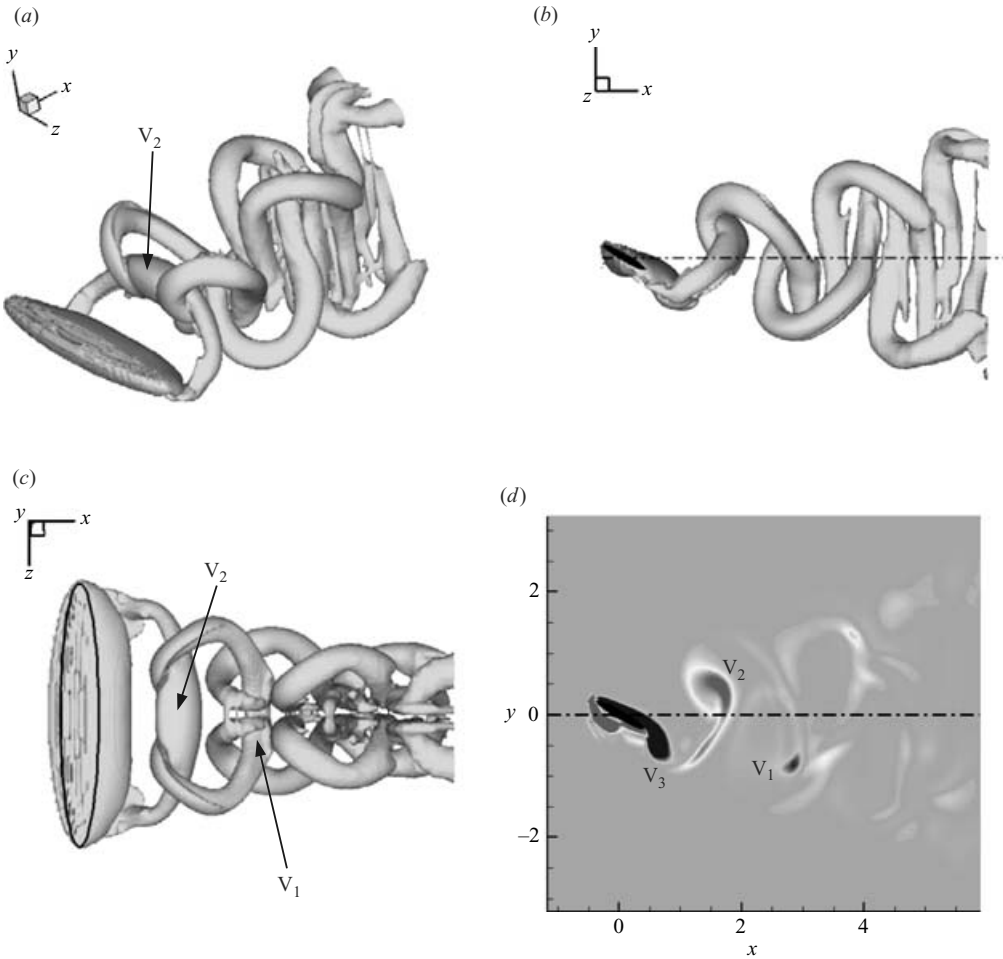
FIGURE 15. Vortex topology for $\mathcal{R} = 5.09$ foil at the phase where foil is at the centre of its heaving motion. (*a*) Perspective view. (*b*) Side view. (*c*) Top view. (*d*) Spanwise vorticity contour plot on spanwise symmetry plane.

narrowing of the wake observed in the previous cases is also visible in the top-view in figure 15(*c*) and as explained before, this is also an effect induced by the tip-vortices.

Figure 16 presents contours of the mean streamwise velocity along the spanwise symmetry plane for this case. The plot shows that topology of the mean wake for this case is quite different from the previous lower-aspect-ratio cases. First, for this case, there is no clear bifurcation of the jet. Instead, we observe a single jet up to about $x/a_x = 2$ and the shape of this jet can be seen in figure 17(*a*). Beyond this point, the jet forms the four-lobed-structure as seen in figure 17(*b*). However, unlike the previous cases, we see that there are also two additional regions of large streamwise velocity on the wake centreline. Further downstream, we observe that the four outer lobes keep spreading in the transverse direction whereas the two regions of high velocity on the wake centreline merge towards the wake centre. Consequently, we see a single region of high streamwise velocity reappear on the wake centreline at around $x/a_x = 6$. The outer four lobes decay rapidly and do not form a bifurcated jet. Instead, we see that the transverse spread of the outer lobes manifests itself as a rapid streamwise
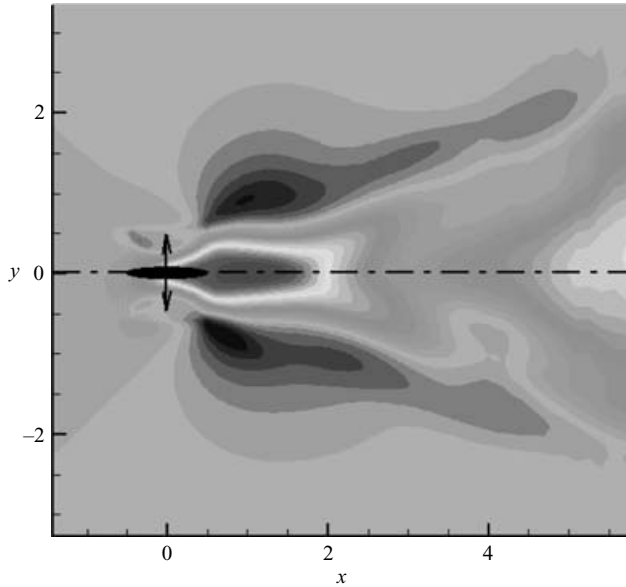
FIGURE 16. Contours of mean streamwise velocity for the $R = 5.09$ case along the spanwise symmetry plan. Contour levels in this plot are the same as those in figure 7.
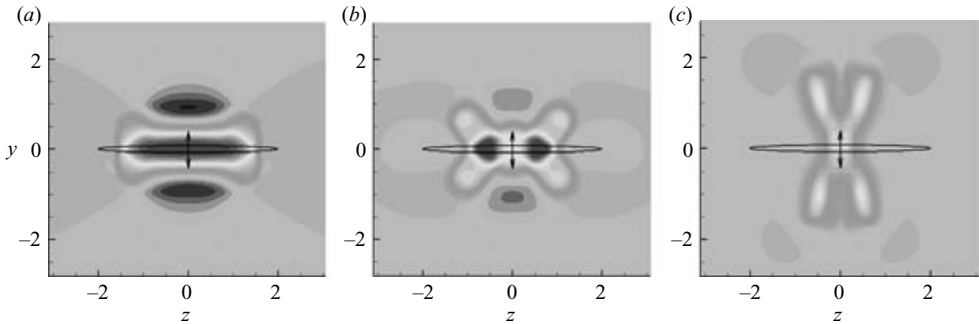

FIGURE 17. Contours of mean streamwise velocity for the $R = 5.09$ case on three streamwise planes in the near wake (*a*) $x/a_x = 1$. (*b*) $x/a_x = 2$. (*c*) $x/a_x = 5$. Contour levels in this plot are the same as the ones in figure 7.

transverse growth of the wake. Thus, this aspect-ratio case is substantially different from the previous lower-aspect-ratio cases. The mean wake in figure 16 is noticeably asymmetric about the wake centreline and this behaviour is inline with that observed for the $R = \infty$ case.

3.1.5. *Effect of key parameters on wake topology*

In this section, we examine the effect of Strouhal number, Reynolds number and pitch-bias on the vortex topology. The discussion in this section is limited to the $R = 2.55$ foil which is the intermediate-aspect-ratio case in the current study and also the one most relevant to fish pectoral fins. First, we focus on the effect of Strouhal number and for this analysis, the Reynolds number is fixed at a value of 200.

Figure 18 presents top views of the vortex topology for $St = 0.4$, 0.8 and 1.2 for this foil and this can be examined in conjunction with the corresponding plot for
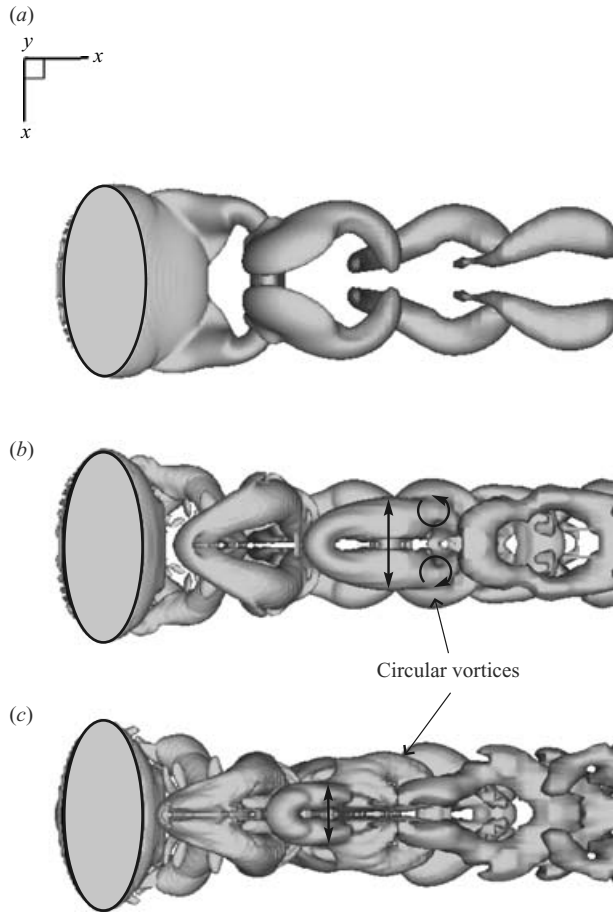
FIGURE 18. Vortex topology for $R = 2.55$ foil for different Strouhal numbers. The Reynolds number is 200 for all these cases. (*a*) $St = 0.4$. (*b*) $St = 0.8$. (*c*) $St = 1.2$.

the $St = 0.6$ case in figure 9. Figure 18(*a*) shows the vortex topology for the Strouhal number of 0.4. The salient feature that must be pointed out here is the absence of any linkage between the tip vortices as seen for $St = 0.6$. This is because the tip vortices formed at this lower Strouhal number have lower strength and this weakens the mutual induction mechanism that is responsible for the linking of the tip vortices as described in § 3.1.2. This observation regarding increased interaction between adjacent vortex loops is also consistent with the simulations of Blondeaux *et al.* (2005*a*, *b*) who find that increase in Strouhal number from 0.175 to 0.35 leads to similar behaviour. The current plot also shows general agreement with figure 5(*b*) in von Ellenrieder *et al.* (2003) where the authors have shown a top-view of the vortex topology for a rectangular $R = 3.0$ foil oscillating at a Strouhal number of 0.4 and Reynolds number of 163. Their plot clearly shows that the wake is dominated by circular vortex loops similar to those seen here.

For the higher Strouhal numbers of 0.8 and 1.2, we observe that as with $St = 0.6$, the tip vortices link together to form spanwise oriented vortex filaments. In fact, at these higher Strouhal numbers, the spanwise spacing of the tip vortices further downstream reduces with increasing Strouhal number as indicated by the arrows
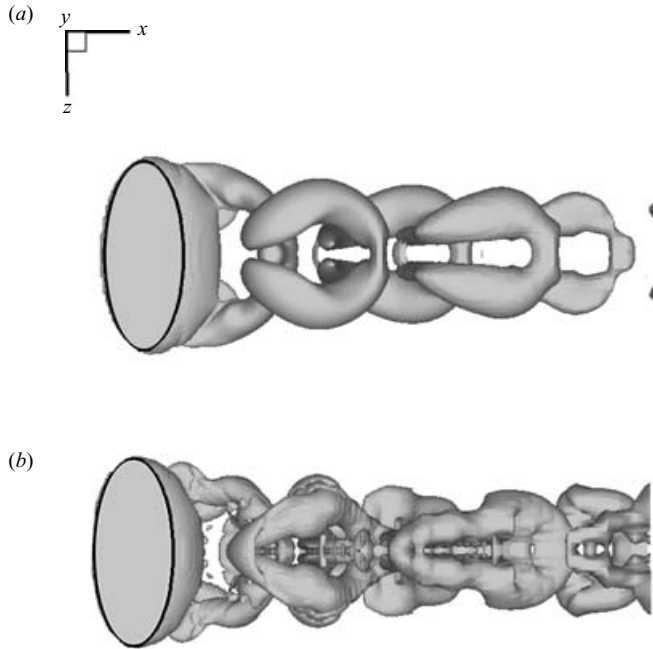
(a)

(b)

Figure 19. Vortex topology for $\mathit{R} = 2.55$ foil for different Reynolds numbers. The Strouhal number is 0.6 for both these cases. (*a*) $Re = 100$. (*b*) $Re = 400$.

in figures 18(*b*) and 18(*c*). This is entirely consistent with our previously described scenario of mutual induction between two sets of tip vortices. Clearly, as the Strouhal number increases, there is a concomitant increase in the tip-vortex strength and their mutual induction leading to the tip vortices moving closer together. Another consequence of the increased strength of the tip-vortices is that these vortices wrap spanwise vortex filaments (wrapping direction indicated in figure 18(*b*) by the circular arrows) around their downstream ends resulting in distinctly circular vortex structures.

In addition to simulations at $Re = 200$ which have been described so far, two additional simulations, one at $Re = 100$ and the other at 400 were carried out for the $\mathit{R} = 2.55$, $St = 0.6$ case in order to assess the effect of Reynolds number on the vortex topology. Figure 19 shows the top-view of the vortex topology for these cases. For the lower Reynolds number of 100, the tip vortices do not join at the upstream end and furthermore, the loops dissipate rapidly in the wake. This behaviour is consistent with the increased viscous effect for this case. The higher-Reynolds-number case, on the other hand, shows many of the features observed for the high Strouhal number case including full upstream merging of the tip vortices, narrowing of the spanwise spacing between the tip-vortices as well as the formation of circular rings like vortices owing to the induction of the tip vortices.

Simulations of the $\mathit{R} = 2.55$ pitching–heaving foil at a higher Reynolds number of 1000 and Strouhal number of 0.6 were also reported in Narsimhan *et al.* (2006). The focus of this study was on CFD-based parameterization of a conceptual bio-robotic autonomous underwater vehicle propelled by flapping foils. The wake at this higher Reynolds number was also found to exhibit a similar topology with two sets of vortex rings propagating at an oblique angle to the wake centreline. Thus it seems
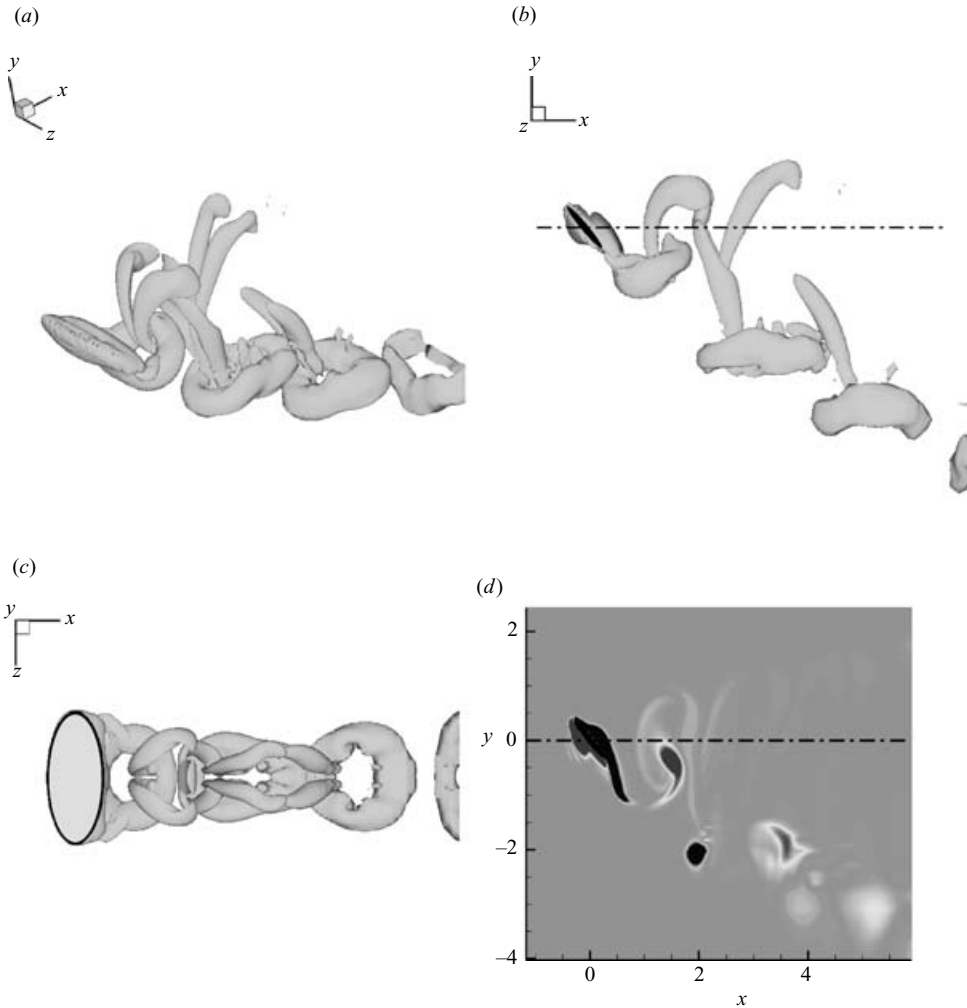
(*a*)

(*b*)

(*c*)

(*d*)

FIGURE 20. Vortex topology for $\theta_0 = 20°$ case. For this case $A\!R = 2.55$, $St = 0.6$ and $Re = 200$.

that the basic vortex dynamics of these finite-aspect-ratio flapping foils is relatively independent over at least an order of magnitude of Reynolds numbers.

Finally, we examine the effect of pitch-bias angle (θ_0) on the wake topology. Pitch-bias has been found to be an effective parameter for producing large mean lift forces for manoeuvring (Triantafyllou, Hover & Licht 2003; Mittal 2004; Singh, Sinha & Mittal 2004). In the current study, we have chosen the case with $A\!R = 2.55$, $St = 0.6$ and $Re = 200$ and have performed simulations for $\theta_0 = 10°$, $20°$ and $30°$ in addition to the zero pitch-bias case described earlier. Figure 20 shows the vortex topology for the $\theta_0 = 20°$ case and this can be compared with the corresponding plots for the zero pitch-bias case shown in figure 9. As expected, introduction of a pitch-bias produces a wake that is strongly asymmetric about the centreline. A strong set of vortex loops and rings is produced below the centreline, whereas the loops formed above the centreline are considerably weaker. Furthermore, the vortex rings in the lower set have their axes oriented almost perpendicular to the streamwise directions and it is expected that this will induce a large downward velocity in this region.

Figure 20(d) shows that if viewed along the spanwise symmetry plane, the lower set of vortex structures appear to form an inverse Kármán-like street that is directed at an oblique angle to the streamwise direction. Thus overall, even with a relatively large bias-angle, many of the essential features of the wake topology remain similar to that observed for the zero-bias angle case.

It is useful to comment on the extent to which some of the hydrodynamic features observed here are also observed in more realistic situations. First, as mentioned previously, the flapping motion is better represented as a pitching–rolling motion. In such a motion there is only one strong tip vortex as opposed to the two tip vortices present for the pitching–heaving foil. However, ongoing simulations of pitching–rolling foils using the same solver show that these foils also produce a series of distinct, but complex, vortex ring-like structures. These vortex structures form from the vortex loops that are generated by the joining of the leading-edge separation vortex (V_3 in figure 8a), the tip vortex and the trailing-edge vortex (V_2 in figure 8a). The induction mechanism responsible for this is analogous to the transformation of vortex loops into vortex rings in the wake of a sphere (Mittal 1999; Mittal *et al.* 2002b). Furthermore, just as in the pitching–heaving case, the vortex rings for pitching–rolling foils arrange themselves into two sets that propagate at oblique angles to the wake centreline. Thus, the essential vortex dynamics described for the pitching–heaving foil are observed in a pitching–rolling foil. Results from this study on pitching–rolling foils will be presented in a separate paper. With regard to the robustness of the wake dynamics observed here, it is worth pointing out that even a pitching panel which does not have a moving leading edge and therefore does not generate a leading-edge vortex, produces a wake which shows many of the features observed here (Buckholtz & Smits 2006).

It should also be noted that previous studies of Drucker & Lauder (1999) which have examined the wake structure of a highly flexible sunfish pectoral fin swimming steadily in an oncoming flow have also indicated the presence of a series of interconnected vortex rings in the wake. Simulations (Lauder *et al.* 2005; Bozkurttas *et al.* 2006) of flow past a sunfish pectoral fin also show that although the wake structure is significantly more complicated owing to the complex shape and deformation of the fin, vortices from the dorsal and ventral edges, and fin-tip do coalesce to form vortex-ring-type structures. Thus, despite the absence of flexibility and the use of a simple canonical foil shape, it seems that the predicted flow does share some rudimentary features with real fins.

3.2. *Hydrodynamic forces*

Figure 21 shows the time variation of the thrust and lift coefficients for various aspect-ratio flapping foils with $St = 0.6$ and $Re = 200$. The plots show the third and fourth cycles in the simulations, by which time the flow has clearly reached a stationary state. For all cases, the thrust peaks twice in each cycle at the time instant in the cycle when the foil is near the centre of its trajectory. Furthermore, the foils experience a maximum drag force just before they reach the extreme points in their heave motion. Although this qualitative behaviour is observed for all the cases, there is a significant reduction in peak thrust with aspect ratio. Specifically, we find that the peak thrust coefficient for the $A\!R = \infty$ is about 1.7, whereas that for the $A\!R = 1.27$ case is about 0.40 which amounts to over a four-fold reduction. Similar observations hold for the lift coefficient where the magnitudes are reduced with aspect ratio, but there is no significant effect on the qualitative characteristics.

Figure 22(a) shows the variation in the mean thrust coefficient with Strouhal number for various aspect-ratio foils at a Reynolds number of 200. First, it can be been
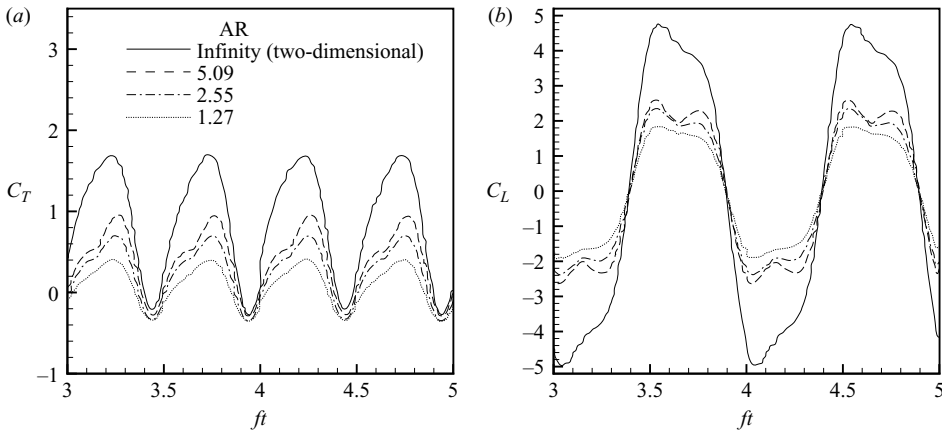
FIGURE 21. Variation of hydrodynamic forces with time for foils of various aspect ratio. (*a*) Thrust coefficient, (*b*) lift coefficient. The Reynolds number is 200 for all these cases.
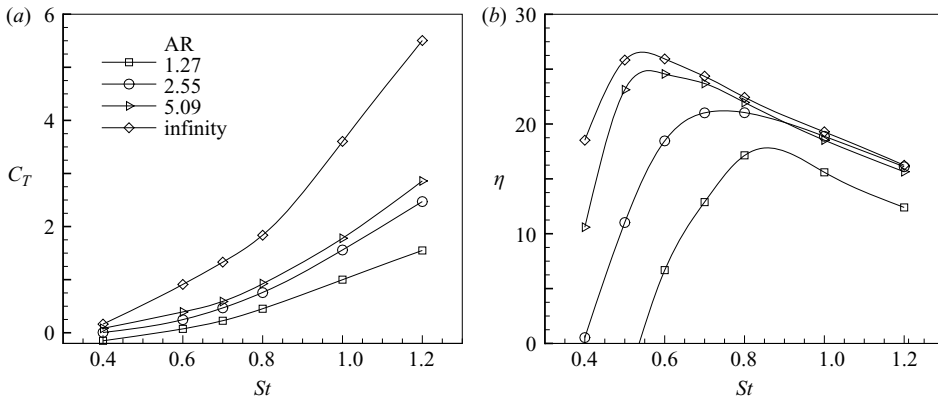

FIGURE 22. Variation of hydrodynamic performance of flapping foils with Strouhal number for for foils of various aspect-ratio. (*a*) Thrust coefficient. (*b*) efficiency. The Reynolds number is 200 for all these cases.

seen from this figure that for all cases, the thrust increases monotonically with the Strouhal number. Such a behaviour is well documented for two-dimensional (infinite-aspect-ratio) flapping foils (Anderson *et al.* 1998; Jones *et al.* 1998; Koochesfahani 1989) and the current simulations prove that low-aspect-ratio foil also shows similar behaviour. At this relatively low Reynolds number, foils produce thrust only at relatively large Strouhal numbers. This is because of the large shear drag that the foils have to overcome at this Reynolds number. In fact, at a Strouhal number of 0.4, the $A\!R = 2.55$ foil produced almost zero net force. Thus, for moderate aspect-ratio foils (such as $A\!R = 2.55$) at these Reynolds numbers, there is a transition from drag to thrust producing behaviour for $St \lesssim 0.4$. This observation has particular relevance for the studies of von Ellenrieder *et al.* (2003) and Blondeaux *et al.* (2005*a*, *b*) since the flow is expected to be quite sensitive to the system parameters and set-up in this transitional regime and could possibly explain the disagreement between the two studies *vis-à-vis* the wake structure.

Figure 22(*b*) presents the variation of efficiency for these cases and a number of trends can be observed in this plot. First, all cases show that the efficiency reaches a
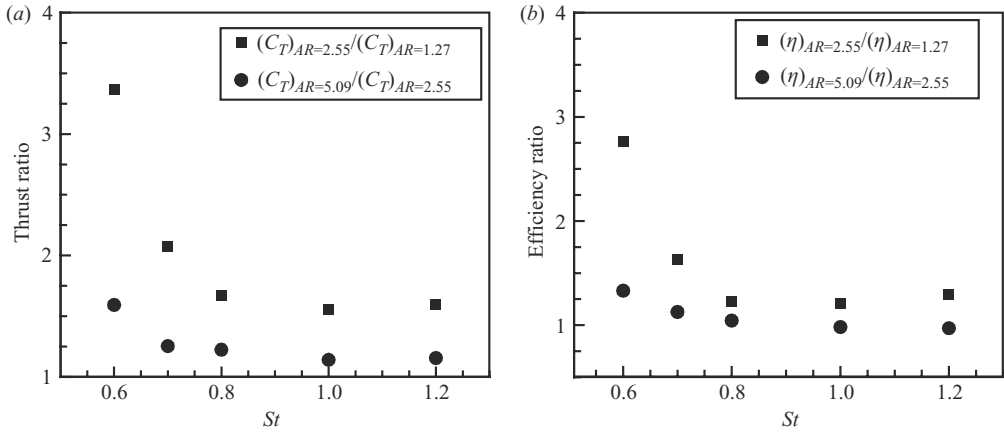
FIGURE 23. Relative increase in hydrodynamic performance with aspect-ratio. (*a*) Thrust coefficient, (*b*) efficiency. The Reynolds number is 200 for all these cases.

maximum at an intermediate value of Strouhal number. Furthermore, the Strouhal number at which this peak occurs decreases with increasing aspect ratio. For the two-dimensional infinite-aspect-ratio case, the maximum is reached at a Strouhal number of about 0.53, whereas the corresponding values of the $AR = 5.09$, 2.55 and 1.27 cases are 0.55, 0.75 and 0.83, respectively. It is also observed that the maximum efficiency increases with aspect ratio. However, at Strouhal numbers higher than about 0.85, all the cases except for the $AR = 1.27$ cases show virtually the same efficiency values. Thus, except for very small aspect-ratio fins, efficiencies comparable to those of a infinite aspect-ratio fin can be attained for higher Strouhal numbers. This would imply that low-aspect-ratio pectoral fins that are used for paddling as well as flapping can match the thrust efficiency of high-aspect-ratio fins in the flapping mode only if the aspect ratio is above a certain minimum value and if the fin is operated at relatively high Strouhal numbers. The optimal Strouhal numbers found in the current study are higher than the range usually considered optimal for swimming and flying animals (Taylor, Nudds & Thomas 2003; Rohr & Fish 2004). This is probably due to the particular choice of parameters (amplitude, maximum pitch angle and Reynolds number) in the current study. As mentioned earlier, the relatively low Reynolds number in the current study leads to a proportionately large shear drag that has to be overcome in order for the foil to produce net thrust. This tends to push optimal Strouhal numbers to higher values. Also, Hover *et al.* (2004) find that even at high Reynolds numbers, depending on the maximum angle-of-attack, the optimal Strouhal numbers can vary from 0.3 to 0.6 for a rigid flapping foil. Thus, the optimal Strouhal number can vary over a fairly large range with some of these parameters.

Figure 23 presents the relative increase in the thrust and efficiency with aspect ratio for a range of Strouhal numbers. Essentially, we compare the relative increase in thrust and efficiency as the aspect ratio doubles from 1.27 to 2.55 with the corresponding increase as the aspect ratio again doubles from 2.55 to 5.09. Values corresponding to $St = 0.4$ are not included in these plots since some of the thrust and efficiency values are close to zero for this Strouhal number and this can give unrealistic values of the relative increase. The plots show that for all Strouhal numbers, the gain in thrust and efficiency in going from $AR = 1.27$ to 2.55 is larger than the corresponding gain in going from $AR = 2.55$ to 5.09. In fact, at the lower end of the Strouhal number range, the difference is quite dramatic. For instance, at $St = 0.6$ the thrust coefficient
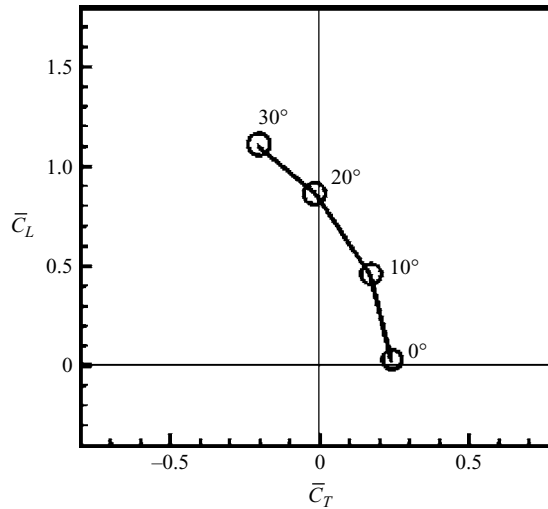
FIGURE 24. Polar plot of mean lift versus mean thrust for various pitch-bias angles. For all three cases in this plot, $R = 2.55$, $St = 0.6$ and $Re = 200$.

increases by a factor of about 3.4 as the aspect ratio increases from 1.27 to 2.55 and the corresponding increase in efficiency is by a factor of 2.75. In contrast, the corresponding factors are 1.6 and 1.3, respectively, for thrust and efficiency when aspect ratio is increased from 2.55 to 5.09. This has some implications for pectoral fins found in nature. Clearly, hydrodynamic considerations alone would tend to lead to pectoral fins with larger and larger aspect-ratios. Conflicting with this tendency are penalties incurred by the animal for bearing large-aspect-ratio fins. These include, but are not limited to, the need for stronger and therefore heavier body structures to withstand the bending moments produced on large-aspect-ratio fins, a larger visual signature associated with longer fins and problems associated with operating long slender fins in tight spaces. The current simulations indicate that significant gains in hydrodynamic performance can be achieved as the fin aspect-ratio is increased to about 2.5. Further increase in aspect-ratio brings only modest gains which could easily be offset by the penalties associated with large-aspect-ratio fins. The above would seem to be equally true for insects and bird wings, but the penalty associated with large bending moments is probably higher for fishes than for insects or birds. This is so because pectoral fins of most fish are designed to be highly flexible, much more so than insect or bird wings. This property of the fins allows for highly complex flapping gaits which the animal uses to manoeuvre and move about in extremely energetic and unsteady environments. Fin flexibility in fish pectoral fins is usually achieved through the use of slender and delicate structural members (such as rays and membranes) which present very little resistance to bending moments. Furthermore, fishes, especially those that employ labriform (pectoral fin) propulsion, usually swim in complex environments such as rocky coasts and coral reefs where the disadvantages of operating long slender fins would be significant. Thus, the pressure against larger-aspect-ratios is probably highest for fish pectoral fins and this, along with the discussion in the previous paragraph provides some explanation for the observation that most fish pectoral fins are found to have an aspect-ratio somewhere between 2 and 3.

For the pitch-bias angle cases, it is useful to examine the effect of this parameter on the thrust and lift production. Figure 24 presents a polar plot of mean lift versus mean

thrust for various pitch-bias angles for the $Æ = 2.55$, $St = 0.6$ and $Re = 200$ case. The plot shows that small changes in the pitch-bias angle can produce relatively large lift forces. In fact, interpolation of this existing data shows that a condition of $\overline{C_L}/\overline{C_T} = 1$ is reached for a pitch-bias angle of about 5°. It should be noted that production of large lift forces would be extremely useful for rapid pitch-up or roll manoeuvres. This effect of pitch-bias is known for two-dimensional flapping foils (Mittal *et al.* 2003; Triantafyllou *et al.* 2003) and the potential use of this parameter for bio-robotic autonomous underwater vehicles has already been explored (Singh *et al.* 2004). The plot also shows that for pitch-bias angles greater than about 20° the foil starts to produce drag. This behaviour is inline with that observed by Triantafyllou *et al.* (2003) for a two-dimensional flapping foils. It should be noted that this drag production at high pitch-bias angles will produce simultaneous braking and turning which would be useful for manoeuvring and/or station-keeping in highly unsteady environments such as littoral regions. Finally, the plot shows that the mean lift continuously increases with pitch-bias angle at least up to 30°. This behaviour is different from that of stationary airfoils. For instance, flow over a NACA 0012 airfoil stalls at an angle-of-attack of about 16° (Abbott 1980). Thus, the flapping motion leads to a dramatic increase in the mean geometric angle-of-attack over which usable lift can be produced.

4. Conclusions

Simulations of flow past thin ellipsoidal flapping foils have been carried out using an immersed boundary solver. In contrast to bird and insect wings, fish pectoral fins tend to be of a relatively lower-aspect-ratio and the current study is an effort to understand the fundamental hydrodynamics of low-aspect-ratio flapping foils. It was also expected that despite the highly simplified kinematics adopted, the current study would lead to some general insights into hydrodynamics of low-aspect-ratio pectoral fin which seem to be common among many species of fish that employ this fin in a flapping-like mode for propulsion.

The simulations show that the wake of thrust-producing finite-aspect-ratio flapping foils is dominated by two sets of interconnected vortex loops and this is consistent with the studies of Blondeaux *et al.* (2005*a*, *b*) and Buckholtz & Smits (2006). For low-aspect-ratios, these vortex loops evolve into distinct non-circular vortex rings as they convect downstream. For all the finite-aspect-ratio cases studied here, the vortex loops/rings convect in a direction which is at an angle to the streamwise direction and this angle is found to decrease with increasing aspect-ratio. The axes of the vortex loops/rings are also found to be oriented at an angle to both the streamwise direction and the direction of their travel. The motion and orientation of these vortex structures lead to the formation of twin oblique jets which are most clearly visible in the time-averaged wake profiles. All of these wake features of foils are described in terms of vortex dynamics. The study also describes the effect of Strouhal and Reynolds number and pitch-bias angle on the wake topology.

Analysis of the hydrodynamic performance of these flapping foils shows that the thrust coefficient increases monotonically with aspect-ratio and Strouhal number for all foils. Furthermore, all foils exhibit a clear maximum in propulsive efficiency with Strouhal number, although it is found that the peak efficiency decreases and the Strouhal number at which this maximum is achieved increases with decreasing aspect-ratio. It is also found that the relative gains in thrust and efficiency are quite large as the aspect-ratio is doubled from 1.27 to 2.55, but the same is not true when the aspect-ratio is doubled yet again. This could partially explain why many of the

pectoral fins found in fish are in the range between 2 and 3. Finally, examination of the mean lift and thrust/drag produced by a finite-aspect-ratio flapping foil with pitch-bias angle shows that even small values of this parameter produce relatively large values of mean lift and this would therefore be a useful parameter for producing manoeuvring forces and moments.

REFERENCES

Abbott, I. H. 1980 *Theory of Wing Sections*. Dover.

Ahmadi, A. R. & Widnall, S. E. 1986 Energetics and optimum motion of oscillating lifting surfaces of finite span. *J. Fluid Mech.* **162**, 261–282.

Anderson, J. M., Streitlien, K., Barrett, D. S. & Triantafyllou, M. S. 1998 Oscillating foils of high propulsive efficiency. *J. Fluid Mech.* **360**, 41–72.

Azuma, A. 1992 *Biokinetics of Flying and Swimming*. Springer.

Blondeaux, P., Fornarelli, F., Guglielmini, L. & Triantafyllou, M. 2005*a* Vortex structures generated by a finite-span oscillating foil. *AIAA Paper* 2005-0084.

Blondeaux, P., Fornarelli, F., Guglielmini, L., Triantafyllou, M. S. & Verzicco, R. 2005*b* Numerical experiments on flapping foils mimicking fish-like locomotion. *Phys Fluids* **17**.

Bozkurttas, M., Dong, H., Mittal, R. & Najjar, F. 2005 Towards numerical simulation of flapping foils on fixed Cartesian grids. *AIAA Paper* 2005-0081.

Bozkurttas, M., Dong, H., Mittal, R., Madden, P. & Lauder, G. V. 2006 Hydrodynamic performance of deformable fish fins and flapping foils. *AIAA Paper* 2006-1392.

Buckholtz, J. H. J. & Smits, A. J. 2006 On the evolution of the wake structure produced by a low-aspect-ratio pitching panel. *J. Fluid Mech.* **546**, 433–443.

Cain, A. B. & Bush, R. H. 1994 Numerical wave propagation analysis for stretched grids. *AIAA Paper* 94-0172.

Cheng, J., Zhuang, L. & Tong, B. 1991 Analysis of swimming three-dimensional waving plates. *J. Fluid Mech.* **232**, 341–355.

Combes, S. A. & Daniel, T. L. 2001 Shape, flapping and flexion: wing and fin design for forward flight. *J. Exp. Biol.* **204**, 2073–2085.

Dickinson, M. H., Lehmann, F. O. & Sane, S. P. 1999 Wing rotation and the aerodynamic basics of insect flight. *Science* **284**, 1954–1960.

Drucker, E. & Lauder, G. 1999 Locomotor forces on a swimming fish: three-dimensional vortex wake dynamics quantified using digital particle image velocimetry. *J. Exp. Biol.* **202**, 2393–2412.

Drucker, E. & Lauder, G. 2002 Experimental hydrodynamics of fish locomotion: functional insights from wake visualization. *Integ. Comput. Biol.* **42**, 243–257.

von Ellenrieder, K. D., Parker, K. & Soria, J. 2003 Flow structures behind a heaving and pitching finite-span wing. *J. Fluid Mech.* **490**, 129–138.

Ellington, C. P. 1984 The aerodynamics of hovering insect flight. ii. Morphological parameters. *Phil. Trans. R. Soc. Lond.* **305**, 17–40.

Fish, F. E., Lauder, G. V., Mittal, R., Techet, A. H., Triantafyllou, M. S., Walker, J. A. & Webb, P. W. 2003 Conceptual design for the construction of a biorobotic AUV based on biological hydrodynamics. In *Proc. 13th Intl Symp. on Unmanned Untethered Submersible Technology (UUST)*. Durham, New Hampshire.

Freymuth, P. 1988 Propulsive vortical signature of plunging and pitching airfoils. *AIAA J.* **23**, 881–883.

Guglielmini, L. & Blondeaux, P. 2004 Propulsive efficiency of oscillating foils. *Euro. J. Mech. B/Fluids* **23**, 255–278.

Hover, F. S., Haugsdal, O. & Triantafyllou, M. S. 2004 Effect of angle of attack profiles in flapping foil propulsion. *J. Fluids Struct.* **19**, 37–47.

ISOGAI, K., SHINMOTO, Y. & WATANABE, Y. 1999 Effects of dynamic stall on propulsive efficiency and thrust of flapping airfoil. *AIAA J.* **37**, 1145–1151.

JONES, K. D., DOHRING, C. M. & PLATZER, M. F. 1998 Experimental and computational investigation of the Knoller–Betz effect. *AIAA J.* **36**, 1240–46.

KOOCHESFAHANI, M. M. 1989 Vortical patterns in the wake of an oscillating airfoil. *AIAA J.* **27**, 1200–1205.

KOTAPATI, R. B. & MITTAL, R. 2005 Time-accurate three-dimensional simulations of synthetic jets in quiescent air. *AIAA Paper* 2005-0103.

LAUDER, G. V., MADDEN, P., HUNTER, I. N., DAVIDSON, J. T., PROCTOR, L., MITTAL, R., DONG, H. & BOZKURTTAS, M. 2005 Design and performance of a fish fin-like propulsor for AUVs. In *14th Intl Symp. on Unmanned Untethered Submersible Technology (UUST)*. New Hampshire.

LEWIN, G. C. & HAJ-HARIRI, H. 2003 Modelling thrust generation of a two-dimensional heaving airfoil in a viscous flow. *J. Fluid Mech.* **492**, 339–362.

LIGHTHILL, S. J. 1975 *Mathematical Biofluiddynamics*. SIAM.

LIU, H., ELLINGTON, C. P., KAWACHI, K., VAN DEN BERG, C. & WILLMOTT, A. P. 1998 A computational fluid dynamic study of hawkmoth hovering. *J. Exp. Biol.* **201**, 461–477.

MITTAL, R. 1999 A Fourier–Chebyshev spectral collocation method for simulating flow past spheres and spheroids. *Intl J. Numer. Meth. Fluids* **30**, 921–937.

MITTAL, R. 2004 Computational modeling in biohydrodynamics: trends, challenges, and recent advances. *IEEE J. Oceanic Engng* **29**, 595–604.

MITTAL, R. & BALACHANDAR, S. 1995 Generation of streamwise vortical structures in bluff body wakes. *Phys. Rev. Lett.* **75**, 1300–1303.

MITTAL, R. & IACCARINO, G. 2005 Immersed boundary methods. *Annu. Rev. Fluid Mech.* **37**, 239–61.

MITTAL, R., UTTURKAR, Y. & UDAYKUMAR, H. S. 2002a Computational modeling and analysis of biomimetic flight mechanisms. *AIAA Paper* 2002-0865.

MITTAL, R., WILSON, J. J. & NAJJAR, F. M. 2002b Symmetry properties of the transitional sphere wake. *AIAA J.* **40**, 579–582.

MITTAL, R., AKHTAR, I., BOZKURTTAS, M. & NAJJAR, F. M. 2003 Towards a conceptual model of a bio-robotic AUV: pectoral fin hydrodynamics. In *13th Intl Symp. on Unmanned Untethered Submersible Technology (UUST)*. Durham, New Hampshire.

NARSIMHAN, M., DONG, H., MITTAL, R. & SINGH, S. N. 2006 Optimal yaw regulation and trajectory control of biorobotic AUV using pectoral fins based on CFD parametrization. *Trans. ASME I: J. Fluids Engng* **128**, 687–698.

PEDRO, G., SULEMAN, A. & DJILALI, N. 2003 A numerical study of the propulsive efficiency of a flapping hydrofoil. *Intl J. Numer. Meth. Fluids* **42**, 493–526.

PREMPRANEERACH, P., HOVER, F. S. & TRIANTAYLLOU, M. S. 2003 The effect of chordwise flexibility on the thrust and efficiency of a flapping foil. In *Proc. 13th Intl Symp. on Unmanned Untethered Submersible Technology (UUST)*. New Hampshire.

RAMAMURTI, R. & SANDBERG, W. C. 2001 Simulation of flow about flapping airfoils using a finite element incompressible flow solver. *AIAA J.* **39**, 253–352.

RAMAMURTI, R. & SANDBERG, W. C. 2002 A three-dimensional computational study of the aerodynamic mechanisms of insect flight. *J. Exp. Biol.* **205**, 1507–1508.

RAMAMURTI, R., SANDBERG, W. C., LOHNER, R., WALKER, J. A. & WESTNEAT, M. W. 2002 Fluid dynamics of flapping aquatic flight in the bird wrasse: three-dimensional unsteady computations with fin deformation. *J. Exp. Biol.* **205**, 2997–3008.

ROHR, J. J. & FISH, F. E. 2004 Strouhal numbers and optimization of swimming by odontocete cetaceans. *J. Exp. Biol.* **207**, 1633–1642.

SANE, S. P. & DICKINSON, M. H. 2001 The control of flight force by a flapping wing: lift and drag production. *J. Exp. Biol.* **204**, 2607–2626.

SINGH, S. N., SINHA, A. & MITTAL, R. 2004 Biorobotic AUV maneuvering by pectoral fins: inverse control design based on CFD parametrization. *IEEE J. Oceanic Engng* **29**, 777–785.

SORIA, J. & CANTWELL, B. J. 1993 Identification and classification of topological structures in free shear flows. In *Eddy Structure Identification in Free Turbulent Shear Flows* (ed. J. P. Bonnet & M. N. Glauser), pp. 379–390. Academic.

SUN, M. & TANG, J. 2002 Lift and power requirements of hovering flight in drosophila virilis. *J. Exp. Biol.* **205**, 2413–2427.

TAYLOR, G. K., NUDDS, R. L. & THOMAS, A. L. R. 2003 Flying and swimming animals cruise at a Strouhal number tuned for high-power efficiency. *Nature* **425**, 707–711.

TECHET, A. H., LIM, K. L., HOVER, F. S. & TRIANTAFYLLOU, M. 2005 Hydrodynamic performance of a biologically inspired 3d flapping foil. In *Proc. 14th Intl Symp. on Unmanned Untethered Submersible Technology (UUST)*. New Hampshire.

TRIANTAFYLLOU, G. S., TRIANTAFYLLOU, M. S. & GROSENBAUGH, M. A. 1992 Optimal thrust development in oscillating foils with applications to fish propulsion. *J. Fluids Struct.* **7**, 204–224.

TRIANTAFYLLOU, M. S., HOVER, F. S. & LICHT, S. 2003 The mechanics of force production in flapping foils under steady-state and transient motion conditions. *Tech. Rep.* MIT Department of Ocean Engineering, Testing Tank Facility Report 031903.

TRIANTAFYLLOU, M. S., TECHET, A. H. & HOVER, F. S. 2004 Review of experimental work in biomimetic foils. *IEEE J. Oceanic Engng* **29**, 585–595.

TUNCER, I. H. & PLATZER, M. F. 2000 Computational study of flapping airfoil aerodynamics. *J. Aircraft* **37**, 514–520.

TUNCER, I. H., WALZ, R. & PLATZER, M. F. 1998 A computational study on the dynamic stall of a flapping airfoil. *AIAA Paper* 98-2519.

UDAYKUMAR, H. S., MITTAL, R., RAMPUNGGOON, P. & KHANNA, A. 2001 A sharp interface Cartesian grid method for simulating flows with complex moving boundaries. *J. Comput. Phys.* **174**, 345–380.

USHERWOOD, J. R. & ELLINGTON, C. P. 2002 The aerodynamics of revolving wings ii. Propeller force coefficients from mayfly to quail. *J. Exp. Biol.* **205**, 1565–1576.

VAN-KAN, J. 1986 A second order accurate pressure correction scheme for viscous incompressible flow. *SIAM J. Sci. Stat. Comput.* **7**, 870–891.

WALKER, J. A. & WESTNEAT, M. W. 1997 Labriform propulsion in fishes: kinematics of flapping aquatic flight in the bird wrasse, gomphosus varius (labridae). *J. Exp. Biol.* **200**, 1549–1569.

WALKER, J. A. & WESTNEAT, M. W. 2000 Mechanical performance of aquatic rowing and flying. *Proc. R. Soc. Lond.* **267**, 1875–1881.

WALKER, J. A. & WESTNEAT, M. W. 2002 Performance limits of labriform propulsion and correlates with fin shape and motion. *J. Exp. Biol.* **205**, 177–187.

WANG, Z. J. 2000 Vortex shedding and frequency selection in flapping flight. *J. Fluid Mech.* **410**, 323–341.

YE, T., MITTAL, R., UDAYKUMAR, H. S. & SHYY, W. 1999 An accurate Cartesian grid method for simulation of viscous incompressible flows with complex immersed boundaries. *J. Comput. Phys.* **156**, 209–240.

ZANG, Y., STREET, R. L. & KOSEFF, J. 1994 A non-staggered grid, fractional step method for time-dependent incompressible Navier–Stokes equations in curvilinear coordinates. *J. Comput. Phys.* **114**, 18–33.